Jakob Schwaiger, BSc

Li-ion transport in ramsdellite $Li_2Ti_3O_7$ probed by impedance spectroscopy

MASTER'S THESIS

to achieve the university degree of
Master of Science (MSc)

Master's degree programme:
Masterstudium Chemie

submitted to
Graz University of Technology

Supervisor

Univ.-Prof. Dr. rer. nat. habil. Martin Wilkening

Institute for Chemistry and Technology of Materials

Graz, July 2025

AFFIDAVIT

I declare that I have authored this thesis independently, that I have not used other than the declared sources/resources, and that I have explicitly indicated all material which has been quoted either literally or by content from the sources used. The text document uploaded to TUGRAZonline is identical to the present master thesis.

EIDESSTATTLICHE ERKLÄRUNG

Ich erkläre an Eides statt, dass ich die vorliegende Arbeit selbstständig verfasst, andere als die angegebenen Quellen/Hilfsmittel nicht benutzt, und die den benutzten Quellen wörtlich und inhaltlich entnommenen Stellen als solche kenntlich gemacht habe. Das in TUGRAZonline hochgeladene Textdokument ist mit der vorliegenden Masterarbeit identisch.

5. August 2025 _____ _____

Date/Datum Signature/Unterschrift

Abstract

Lithium titanium oxides have been studied extensively as potential anode material in lithium-ion batteries, due to their superior capacity and stability during charging and discharging. Among these compounds, ramsdellite $Li_2Ti_3O_7$ is of particular interest because of its channel-like structure, which is believed to enable quasi-one-dimensional lithium-ion transport. Despite its promising structural features, an in-depth analysis of both long- and short-range Li^+ transport processes within the material is lacking. Therefore, impedance data of ramsdellite $Li_2Ti_3O_7$ were analysed in this thesis. The measurements covered a frequency range from 10 mHz to 3 GHz at temperatures from –100 to 200 °C. Two diffusion processes, long-range and short-range, respectively, were identified by analysing conductivity isotherms and modulus spectra. Moreover, activation energies for each process were derived from Arrhenius plots and Nyquist plots were used to determine the corresponding capacitances. Based on the extracted capacitances, the long-range process was attributed to lithium-ion diffusion across grain boundaries, while the short-range process was identified as Li^+ transport within the bulk regions of the sample. In addition, a third process in the high-frequency range (0,4 GHz) was detected but could not be clearly attributed to ion diffusion. The signal likely results from lattice vibrations or an artefact of the measurement. Although the expected one-dimensional nature of the bulk process was not confirmed by the applied Jonscher fits, the results obtained in the frame of this thesis nevertheless point to low-dimensional diffusion. They are consistent with established structural models found in literature and provide a conclusive insight into the lithium-ion transport in ramsdellite $Li_2Ti_3O_7$, serving as a starting point for further investigations.

Content

1 Introduction

According to their report `World Energy Outlook 2024´, the international energy agency (IEA) expects a significant annual increase in the global demand for electricity of 3 %.[1] This trend is due to both economic and environmental pressure to phase out the reliance on fossil fuels.[2,3] Another important aspect is the surge of new technologies in the digital field such as artificial intelligence, which require additional, energy intensive data centres.[4] While electricity production is vital for this transformation, so is the creation of the related energy infrastructure. Amongst other things, advanced energy storage devices are of great importance, with the IEA predicting that batteries produced globally in 2030 will have to provide 3880 GWh of electrical energy.[1] This means a nearly 360 % increase compared to 2023. Research teams around the world are determined to contribute to this change. Their scientific work has provided a wide range of potential battery components, which is daily extended and optimized further in the quest for new battery materials with superior properties (vgl.[5]). While factors like scale-up possibilities and cost efficiency are important at a later stage, the investigation of (electro)chemical and physical processes on a macroscopic as well as microscopic scale lays the foundation of these efforts. A deeper understanding of the link between fundamental interactions in the material and their desired properties is essential. It leads the way to both new concepts and targeted optimization in the field of energy storage, enabling us quite literally to empower future generations.

Nowadays, state-of-the-art lithium-ion batteries (LIBs) use graphite as anode material due to its low cost and high reversibility.[6] However, a major downside of graphite anodes are volume changes during the intercalation process of Li ions. These lead to a reduction in capacity over the lifetime (charge-discharge cycles) of the battery, caused by cracking of the material.[7,8] In this regard, lithium titanium oxides (LTOs) are promising alternative anode materials, providing a good cycling stability combined with other preferable properties like high thermal stability and environmental friendliness.[9] Additionally, the formation of metallic lithium dendrites, which poses a safety risk in their graphite counterparts, can be avoided in LTOs.[10] A setback are their low electronic conductivities and slow ion diffusion, limiting the practical capacity at large charge-discharge rates. Different approaches are currently investigated to

solve this problem (e.g. doping, increasing the ion concentration or the number of additional defects).[8] One of the compounds, $Li_2Ti_3O_7$, has a metastable form with ramsdellite structure, first synthesized in 1957. As the material´s structure contains parallel channels, it has been suggested that lithium ions diffuse mainly along these channels, making ramsdellite $Li_2Ti_3O_7$ a quasi-one-dimensional (1D) ion conductor.[11–13]

The advantages of understanding lithium-ion diffusion processes in ramsdellite-type $Li_2Ti_3O_7$ (hereafter referred to as $Li_2Ti_3O_7$) are two-fold. On the one hand, it contributes to the research field of applied LTO anode materials for energy storage. $Li_2Ti_3O_7$ has been found to be an excellent material for lithium insertion, showing good cyclability as well as low polarization during the charging and discharging process.[14,15] On the other hand, it serves as a model system for quasi- 1D lithium diffusion, a concept that can be translated to the design of future advanced LIBs. While two-dimensional (2D) diffusion processes in materials have been extensively studied (e.g. the already mentioned graphite)[7,16], significantly fewer examples of 1D diffusion in materials are known so far.[17] The potential benefit of such 1D systems lies in the high mobility of intercalated lithium ions, resulting in superior ion conductivity.[18] For this reason, numerous investigations have been conducted over the last decades. The main objective has been to determine the location of the mobile lithium ions inside the titanate framework as well as their migration paths through the system. While a variety of experiments and calculations were performed on the matter of $Li_2Ti_3O_7$[11,19], an in-depth analysis of the short- and long-range ion transport processes is missing. In the present thesis, datasets obtained by impedance spectroscopy measurements of a powder sample of $Li_2Ti_3O_7$ are analysed. The raw data were obtained by former members of this research group.[20]

2 Theoretical Background

2.1 Diffusion processes in solids

The information for this general overview of diffusion was taken from the first four chapters of the book `Diffusion in solids' by Helmut Mehrer[21], if not stated otherwise.

2.1.1 Diffusion in general

In 1855, A. Fick proposed a concept to describe a diffusion process as a linear response acting in opposition to a concentration gradient.[22] Although his idea was based purely on experimental observations, it is still considered valid after over one and a half centuries of scientists gathering additional insight into the field of diffusion. The equation

2-1 $$J_x = -D \frac{\partial C}{\partial x}$$

is known as *Fick´s first law*. It states that the flux J_x of particles in x-direction is proportional to the first derivative of the concentration C of the particles with respect to x, multiplied by the diffusion coefficient D, which is not further specified at this point. The negative sign is due to the diffusion working against the concentration gradient, as already mentioned. The equation can further be extended to describe a three-dimensional model by using the *nabla symbol* ∇ to define a time-dependent gradient field $C(x, y, z, t)$. This leaves us with

2-2 $$J = -D \nabla C$$

Fick´s first law defines diffusion as the flux of particles through space, neglecting the time-dependence of the process. If the concentration within a finite space change over time (meaning the particle uptake via diffusion does not match the number of outgoing particles), this can be described via a divergence operator ∇, that is applied to the flux in three dimensions

2-3 $$-\nabla J = \frac{\partial C}{\partial t}$$

When combining equation 2-2 and 2-3, we arrive at *Fick´s second law*, also named *diffusion equation,* a partial differential equation of the second order

2-4 $$\frac{\partial C}{\partial t} = \nabla\,(D \nabla C)$$

In case the diffusion does not depend on the concentration, we get a linear diffusion equation. By using the Laplace operator Δ, this can be written as

2-5 $$\frac{\partial C}{\partial t} = D\,\Delta\,C$$

2.1.2 Random walk theory

The random walk theory considers the diffusion of a particles as a series of consecutive movements from one position to another. The overall change in the particles´ position can be described as the sum of these individual movements. Within solids, the movements are limited to the transition between energetically favourable locations in the structure, which atoms therefore predominantly occupy. Within a crystal lattice, there are defined distances λ between these sites. The random walk of an atom within a crystal structure is illustrated in Figure 1.

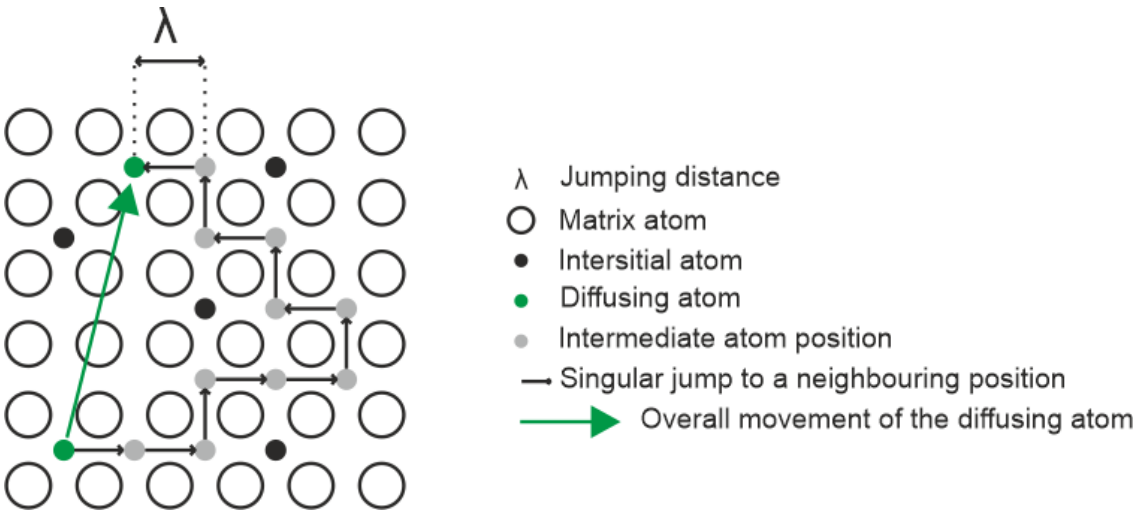

Figure 1: The random walk theory in the case of solids describes the diffusion of an atom (green) as sequence of individual jumps to neighbouring crystal sites (black arrow). The overall movement of the atom (green arrow) can be seen as the sum of these jumps. Figure inspired by reference 21.

Movements of an atom or ions from one crystal site to another are called jump processes and the frequency with which they occur is defined as jump rate Γ (alternatively τ^{-1}). Consequently, the diffusion in a crystalline material depends on these parameters. As mentioned earlier, the flux J is defined as sum of the incoming and outgoing particles. For an individual crystal site, it is therefore composed of jump processes towards and away from the position. The number of diffusing atoms in the flux depends on the jump rate (frequency of transitions) and the concentration (number of atoms in a position to reach the site). As the concentration for its part is related to the distance between the sites, some substitutions and a Taylor series allows the definition of the flux for one dimension as

2-6
$$J_x = -\lambda^2 \Gamma \frac{\partial C}{\partial x}$$

In connection with *Fick´s first law* (*2-1*), the relation between the diffusion coefficient and the jump parameter can be formulated as

2-7
$$D = \lambda^2 \Gamma$$

It is important to note that these assumptions are valid for uncorrelated jump processes. In case of correlations (i) between the jumping atom/ions and (ii) the jumping atom and its surroundings (e.g. vacancies left by a jumping atom would enhance the probability of a return jump), it is necessary to add a correlation factor f to account for such interactions.

2.1.3 Jumping theory

The jumping theory suggests that an atom is located at a crystal site A and separated from the neighbouring site B by a potential barrier, which is due to repulsive forces from surrounding atoms. They create a field potential that needs to be overcome for a transition from A to B (or vice versa). During the transition phase, the least favourable position for the diffusing atom in terms of its potential energy is marked as saddle point. In the energy diagram, it defines the energy required for the jump process. The potential difference between the equilibrium position A and the saddle point is the activation energy (E_a). This is depicted in Figure 2.

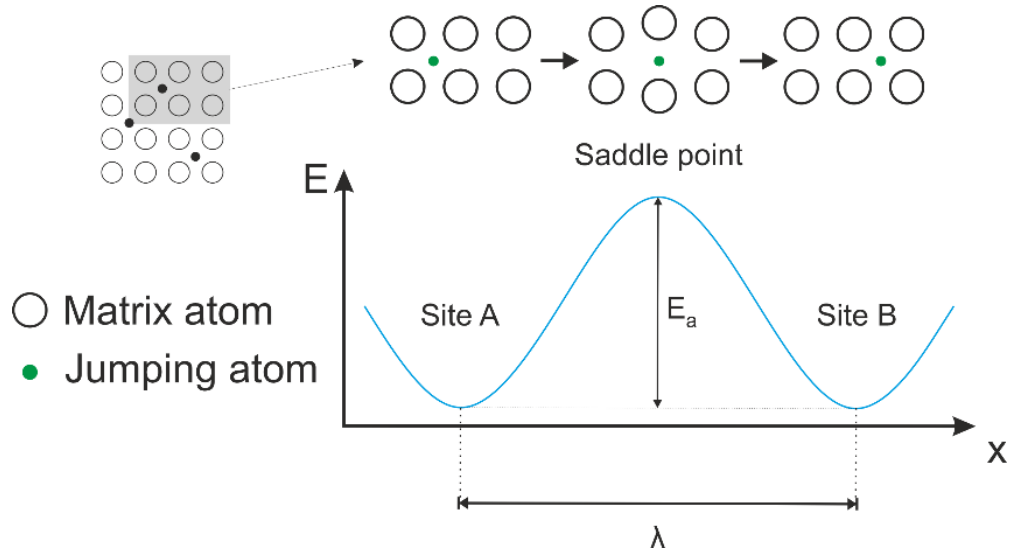

Figure 2: The jump process of an atom (green) between two - in this case energetically equal - sites A and B can be seen in the upper part of the figure. Below, the potential landscape in jumping direction is depicted. To perform a successful jump, an atom has to overcome the energy barrier E_a. Its peaks (saddle point) is the energetically least favourite position from the atom closest to the surrounding matrix atoms. Figure inspired by reference 21.

The atom at site A in our model possesses a thermal energy $k_B T$, (k_B being the *Boltzmann constant* in Joule per Kelvin and T the temperature in Kelvin) and is therefore vibrating around its equilibrium position. At finite temperatures, the mean kinetic energy of the atom is lower than the energy barrier, which means that most of the vibrations do not lead to a transition. The jump rate Γ is therefore much smaller than the vibration frequency ν_0. For our model, we consider the vibrations in the direction of the saddle point and can also refer to it as the attempt frequency (as in attempts to overcome the energy barrier). With the jump rate depending on the height of the energy barrier (the activation energy) and the temperature, we can formulate an Arrhenius law for the jump rate Γ:

2-8
$$\Gamma = \nu_0 \exp\left(-\frac{E_a}{k_B T}\right)$$

2.2 $Li_2Ti_3O_7$ with ramsdellite structure

With a high theoretical specific capacity of 235 mAh g^{-1} in combination with a low average insertion voltage of 1.5 V, $Li_2Ti_3O_7$ with ramsdellite-structure shows promising properties for a use as anode material in lithium-ion batteries.[14,15] According to electrochemical studies by Garnier *et al.*[23], the electronic contribution to the overall conductivity is negligible, hence, $Li_2Ti_3O_7$ can be viewed as a purely ionic conductor. The ramsdellite structure of $Li_2Ti_3O_7$ was first described by Morison and Mikelsen.[24] It crystallises in the space group *Pbnm* and consists of edge- and corner-sharing TiO_6 octahedra, with lithium ions (Li^+) occupying the tetrahedral voids, as depicted in Figure 3. Within these voids, positions of Li^+ can be further separated into 4c and 8d sites.[11] While the exact location of Li^+ is important for a deeper understanding of the diffusion mechanism, a detailed discussion lies beyond the scope of this thesis.

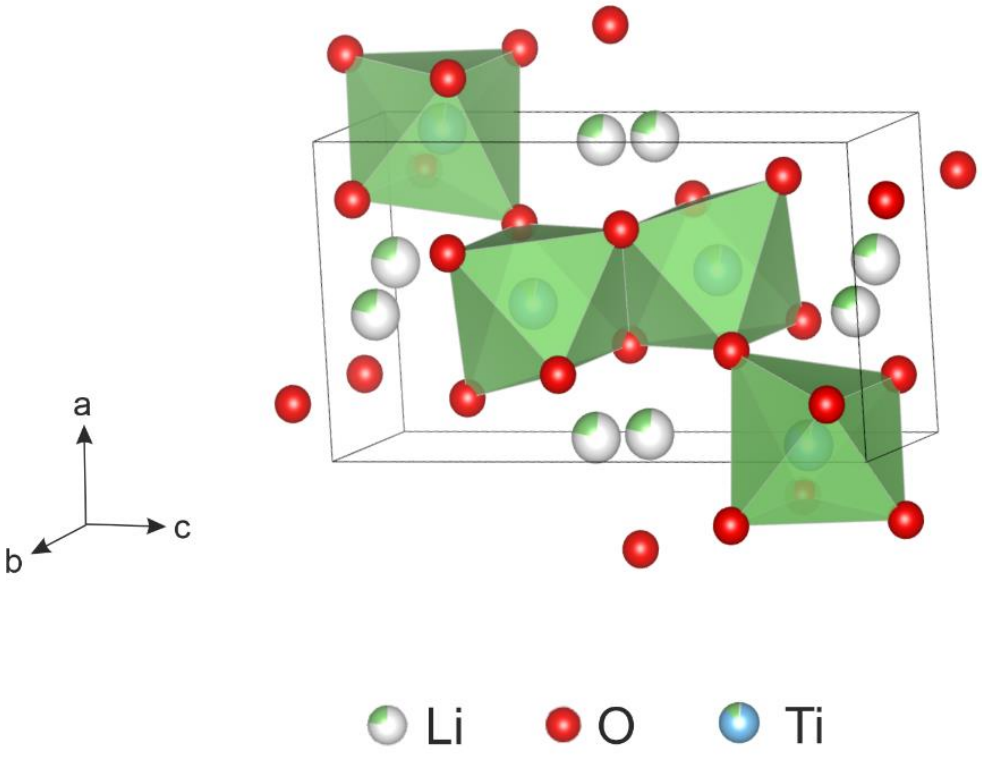

Figure 3: Unit cell of ramsdellite $Li_2Ti_3O_7$. The structure consists of a TiO_6 framework (green octahedra) with lithium ions located in the tetrahedral voids in between. The crystallographic data for the illustration were taken from reference 25.

Ever since the structure was defined, exact distribution of lithium in the framework was subject to multiple studies. While Abrahams *et al.*[12] proposed a structure where lithium can occupy both tetrahedral and octahedral sites, giving the formula $[Li_{1.5}\square_{5.5}]_i[Li_{0.5}Ti_3]_fO_7$. In more recent studies, it was shown that the octahedral positions might not be occupied, suggesting a $[Li_2\square_5]_i[(Ti_3\square_{0.5})_fO_7$ structure.[18,19] As Li^+ ions are limited to tetrahedral sites according to this model, it follows that the lithium diffusion occurs via jump processes between these sites. The tetrahedral sites are forming channels within the material along the b-axis, as illustrated in Figure 4. It is therefore assumed that Li^+ predominantly move through these channels, making $Li_2Ti_3O_7$ a quasi-1D ionic conductor.

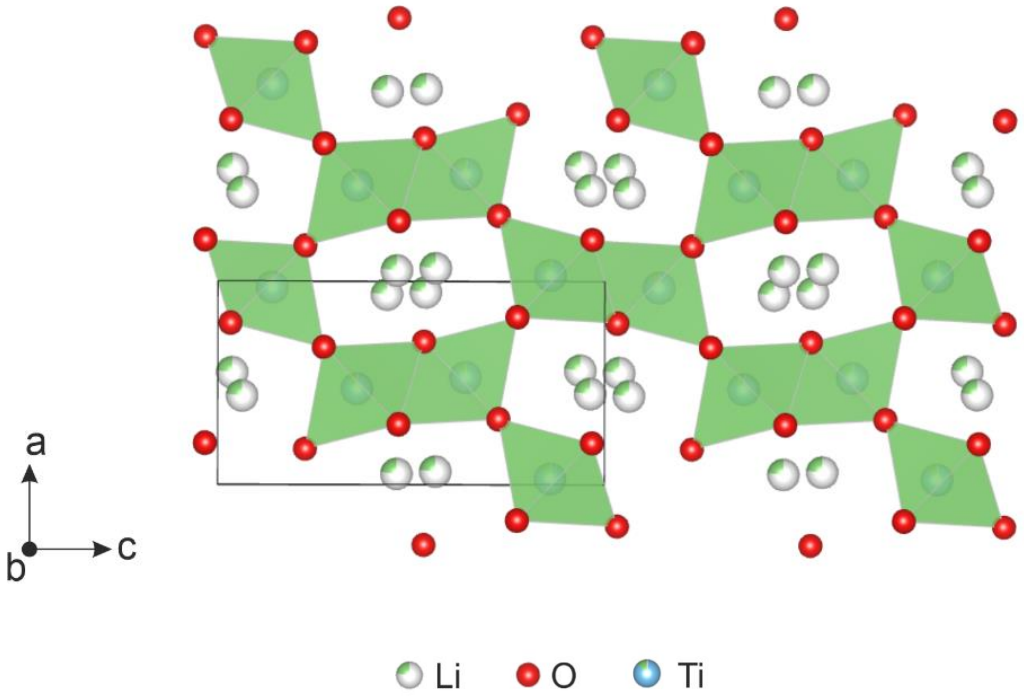

Figure 4: Cross-section of the ramsdellite structure along the ac-plane illustrating the channels along the b-axis, allowing for quasi- 1D lithium diffusion in $Li_2Ti_3O_7$. Structural data taken from reference 25.

Theoretical calculations by Islam *et al.*[11] suggest that while diffusion is preferably happening along the b-axis, Li^+ ions can also migrate between neighbouring tunnel structures via octahedral vacancies. Although this jump process is possible, it is not (energetically) favourable. Consequently, detecting Li^+ in octahedral positions in experimental setups is challenging, as the occupation is very short lived and is infrequent compared to diffusion along the channels.

2.3 Methods

2.3.1 X-ray powder diffraction (XRPD)

X-ray diffraction is an analytical method that uses the scattering of X-ray radiation on a sample to derive information about its molecular structure from the reflections. In the case of X-ray powder diffraction (XRPD) measurements, X-rays are directed on a powder sample and the scattered X-ray radiation is detected. Due to variations in path lengths of the beam, scattering at different crystal planes of in the sample results in phase shifts of the X-rays which vary with the distance between these planes, depicted in Figure 5. This leads to characteristic reflection patterns, arising from constructive and destructive interference, depending on the scattering angle θ.[26]

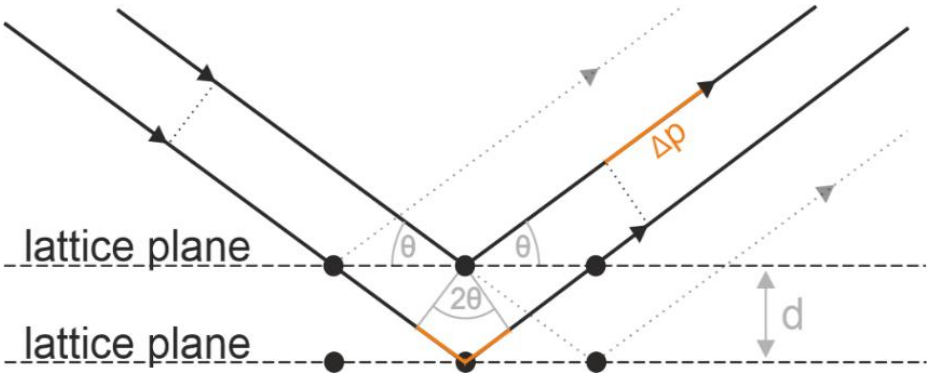

Figure 5: The principle of X-ray diffraction (XRD) is based on differences in the path lengths of X-rays - directed at as sample at an angle θ - which are scattered on atoms within a crystal structure. These differences (Δp; orange) induce a phase shift of the X-rays that varies with the distance d between the crystal planes. Figure inspired by reference 26.

From the characteristic reflection patterns at the detector, it is possible to deduce information about the crystal structure. The principle is based on *Braggs law*, which relates the reflection´s intensity maxima to the spacing between crystal planes in the sample

2-9 $$n\lambda = 2d\sin\theta$$

where *n* is a positive integer, *λ* is the wavelength of the X-ray beam, *d* is the distance between the lattice planes and θ is the angle between the incoming (as well as scattered) X-rays and the lattice plane.[26]

The diffraction pattern depends on a variety of aspects, such as crystal structure, atom sizes, stoichiometric composition and the presents of impurities. It is characteristic for a given material and can be used for identification by comparing the measured pattern to a reference diffractogram. The intensity of the reflection gives insights into the sample's morphology. A higher crystallinity leads to enhanced reflections, as more crystal planes are well-aligned within the sample. However, the specific relations will not be discussed further here. Detailed information can be found for example in the book on X-ray crystallography by M. Woolfson.[26]

2.3.2 Impedance spectroscopy

Electrochemical impedance spectroscopy (EIS) probes the impedance of a sample to get information on sample specific properties like conductivity. This can be used to get insights into the long-range transport of charge carriers within the sample. For the measurement, an alternating voltage *U* is applied to a sample and the answering alternating current *I* of the so formed circuit is recorded. The setup of the measurement can be seen in Figure 6.

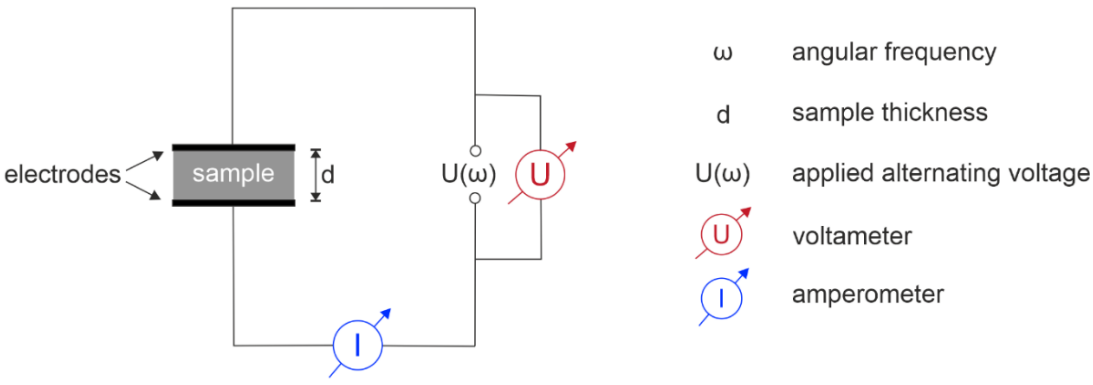

Figure 6: The sample is placed inside an electrical circuit, to which an alternating voltage U is applied. The current I of the circuit is then measured. From the difference between U and I, one can deduce information about the impedance of the material. Figure inspired by reference 21.

Both voltage and current can be defined by their amplitudes and the angular frequency. Additionally, the recorded answering current may exhibit a phase shift φ relative to the applied voltage.[27]

2-10 $$U(t) = U_0 \sin(\omega t)$$

2-11 $$I(t) = I_0 \sin(\omega t - \varphi)$$

Consequently, the deviation of the current from the applied voltage can be two-fold: On the one hand, a change in amplitude (ΔA) is caused by the resistance *R* of the sample material. One the other hand, its capacitance *C* leads to a phase shift by an angle ϕ. This is illustrated in Figure 7 A.

Analog to Ohm's law, the impedance *Z* of a material can be calculated by dividing the voltage by the current

2-12 $$Z = \frac{U_0 \sin(\omega t)}{I_0 \sin(\omega t - \varphi)} = |Z| \frac{\sin(\omega t)}{\sin(\omega t - \varphi)} \text{ with } \frac{U_0}{I_0} = |Z|$$

In contrast to the resistance for direct current (DC), the impedance can also be depicted as a complex number, due to its frequency-dependence. In combination with Euler´s relationship $exp(i\varphi) = cos\varphi + i * sin\varphi$, we get *Z** as the sum of a real part *Z´* and an imaginary part *Z´´*

2-13 $$Z^* = |Z| \frac{e^{i(\omega t)}}{e^{i(\omega t - \varphi)}} = |Z| e^{i\varphi} = |Z|(\cos\varphi + i\sin\varphi) = Z' + iZ''$$

Z´ is hereby representing the resistance of the material, analogue to *R* for DC. *Z´´* represents capacitive contributions. By plotting the imaginary part of the impedance against its real part, one can visualize changes of the current with respect to the applied voltage. The real part depicts the resistance in the sample, while the imaginary part represents the capacitive contributions. The angle δ, complementary to the phase shift φ, is called dissipation or loss angle and indicates the loss of current due to resistance, compared to its temporary reduction via capacitive effects (Figure 7 B).[28]

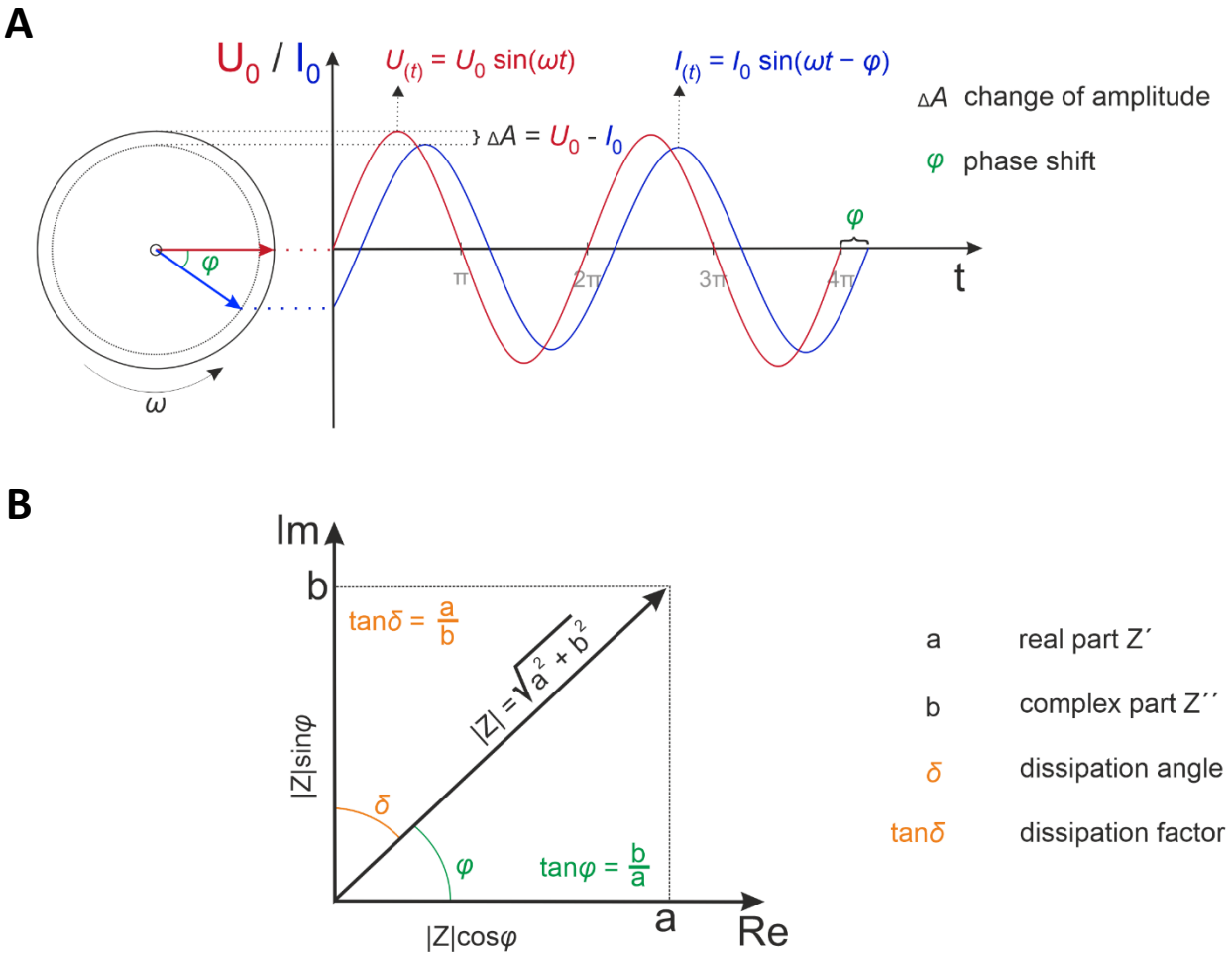

Figure 7: Principle of impedance measurement. ***A*** *The deviation of the current from the applied voltage can result in the change in amplitude (ΔA) or a phase shift by an angle φ.* ***B*** *By plotting the imaginary part of the impedance (b) against its real part (a), one can visualize changes of the answering current. Figure inspired by reference 27.*

2.3.2.1 Conductivity isotherms

The complex conductivity σ^* of a material is indirectly proportional to the impedance and takes the geometry of the sample into account, with A as the cross-section area and h as the sample height (thickness).

2-14 $$\sigma^* = \frac{1}{Z^*}\frac{h}{A}$$

To depict the conductivity isotherms, the logarithm of the real part σ' of the conductivity is plotted against the frequency on a double logarithmic scale, as shown in Figure 8. While the conductivity increases with temperature, its dependence on frequency is more complex. It can be divided into three general regimes:

I. Electrode polarization:

At lower frequencies, the time frame is sufficiently long for ions to migrate toward the electrode before the direction of the voltage switches. As the ions cannot penetrate the electrode material, they accumulate at the interface. The charge transfer is limited to electronic contributions of the current, which leads to a decrease in conductivity. This is referred to as electrode polarization.

II. DC plateau:

At intermediate frequencies, the conductivity of the sample becomes independent of frequency. This causes the movement of electrons and ions without a capacitive component, showing the purely resistive behaviour of the direct current. The so formed frequency-independent region in the plot is called DC plateau. Its conductivity σ_{DC} is derived from long-range transport of ions in the sample, taking their successful ion jumps into account. Each plateau observed in the conductivity isotherm can correspond to a distinct diffusion process in the material.

III. Dispersive regime:

At higher frequencies, the time frame is too short for ions to complete jump processes between two crystal sites. As a result, all ionic motions —including both successful and unsuccessful forward and backward jumps— contribute to the measured conductivity. Unlike the DC plateau, where only long-range, successful ion jumps are reflected. Consequently, the conductivity increases in the dispersive regime, as short-range localized motions dominate this region.

In addition, the regimes shift towards higher frequencies with rising temperature. This can be relevant for temperatures significantly higher or lower than those depicted in Figure 8, as DC plateaus might not be visible in the measured frequency range.

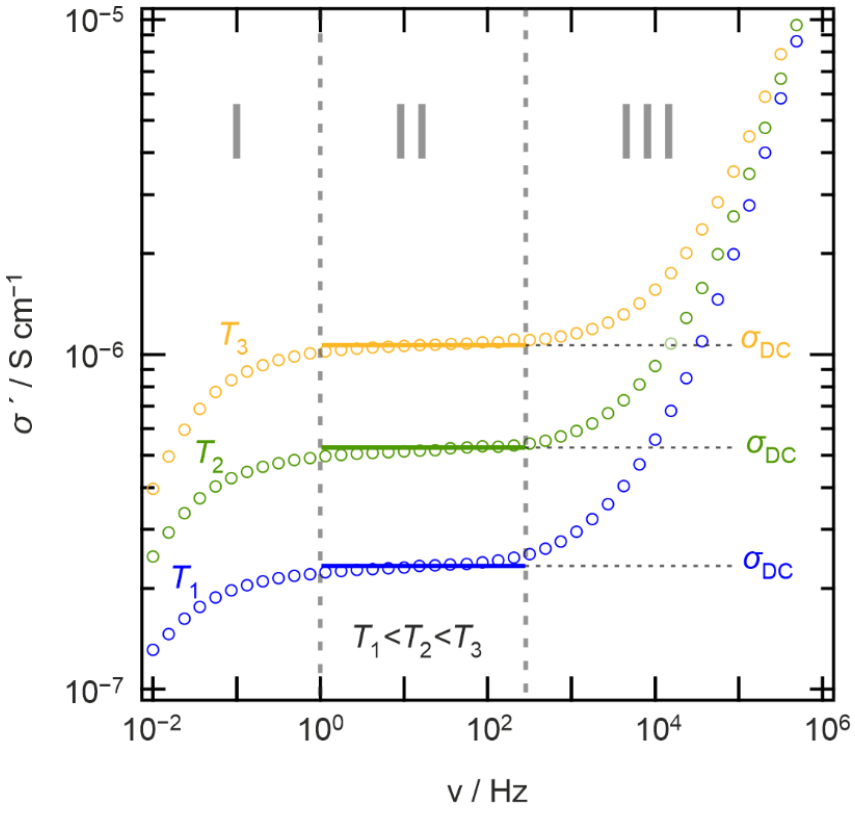

Figure 8: The conductivity isotherms show the real part of the conductivity at three different temperatures in the frequency range from 10 mHz to 1 MHz. They can be separated into three regimes, the electrode polarization (I), defined by the polarization effect of the electrode, the DC plateau (II), where the conductivity is frequency-independent and a dispersive regime (III) which is governed by localized motion of the ions.

The activation energy (E_a) can be derived from the conductivities σ_{DC} at the DC-plateaus. This is possible via the Arrhenius law for the conductivity

2-15 $$\sigma_{\mathrm{DC}} = \frac{\sigma_0}{T} \exp\left(\frac{-E_a}{k_B T}\right)$$

When the product of temperature and σ_{DC} is plotted on a logarithmic scale against the inverse temperature, E_a can be determined via the slope of a linear fit from the data points in the so formed Arrhenius plot:

To calculate the activation energy, equation 2-15 transformed, resulting in

2-16 $$\log(\sigma_{DC} T) = \log(\sigma_0) - \log(e)\, E_{\mathrm{a}}\, \frac{1}{\mathrm{k_B} T}$$

and further in

2-17 $$\log(\sigma_{DC} T) = \log(\sigma_0) - \log(e)\, E_{\mathrm{a}}\, \frac{1}{1000 \mathrm{k_B}}\, \frac{1000}{T}$$

which can be depicted in an Arrhenius plot. The data points are then fitted with a linear function of the form

2-18 $$y = kx + d \quad \text{with } x = \frac{1000}{T}$$

According to this, one can write the slope k of the line as

2-19 $$k = -\log(e)\, E_{\mathrm{a}}\, \frac{1}{1000\, \mathrm{k_B}}$$

Solving for the activation energy, one finally arrives at

2-20 $$E_{\mathrm{a}} = -1000\, k\, \mathrm{k_B}\, \frac{1}{\log(e)}$$

2.3.2.2 Jonscher fits

In 1977, A. Jonscher proposed an `universal power law' to describe the dielectric response of solid materials to an applied AC current.[29] His observations are based on empirical data and allow a fit (Jonscher fit) for the conductivity of the DC plateaus and in the dispersive regimes, using an power law equation. In case of ionic conductors, the law can be approximated to

2-21 $$\underline{\sigma'} = \sigma_{\mathrm{DC}}\left[1 + \left(\frac{\nu}{\nu_c}\right)^n\right] \text{ with } \nu_c = \nu \text{ at } 2\sigma_{\mathrm{DC}}$$

with ν_c being the crossover frequency, the transition frequency from the DC plateau to the dispersive regime, and n being the power law exponent. By fitting the conductivity isotherms with the power law function as depicted in Figure 9, it is possible to derive ν_c — the frequency at which the conductivity is two times σ_{DC} — and n for each temperature.

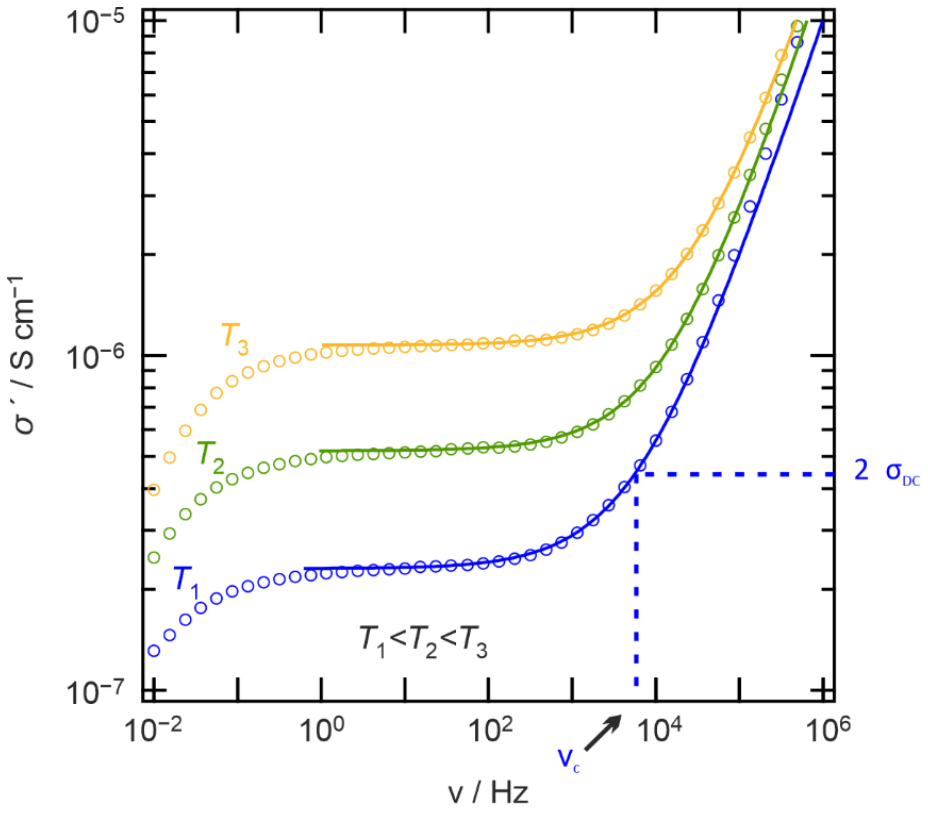

Figure 9: Isotherms fitted by Jonscher´s power law. The crossover frequency ν_c is the frequency at which the conductivity is two times σ_{DC}.

It could be shown that the power law exponent *n* has an empirical dependence on the dimensionality of conductivity dispersion in ionic materials.[30] Isotherms of 3D conductors can be fitted using exponents between 0.9 and 0.6, while fits for 2D and 1D conductors have exponents in the range of 0.6 to 0.4 and below 0.4, respectively.[31]

Analog to the product $\sigma_{DC}\,T$ for isotherms, crossover frequencies ν_c derived from the Jonscher fits can be used to determine the E_a of processes via an Arrhenius plot, using

2-22 $$\nu_c = \nu_{c0}\exp\left(-\frac{E_a}{k_B T}\right)$$

2.3.2.3 Modulus

The modulus is another, unitless form to describe the data gathered by impedance measurements. In contrast to conductivity isotherms, which are sensitive to processes with a high resistance, the imaginary modulus highlights processes with low capacitance. It is calculated via the equation

2-23 $$M^* = \frac{i\omega\varepsilon_0}{\sigma^*}$$

with ω as the angular frequency and $\varepsilon_0 = 8{,}854\cdot10^{-12}$ F/m being the vacuum permittivity. When the imaginary part of the modulus (M'') is plotted against the frequency, the number of peaks (M''_{max}) for each temperature indicates the number of ion transfer processes in the material. Moreover, the height of a peak in the plot is depending on the type of process.[32] From the peak height it is possible to derive the capacitance *C* of the respective process via the equation

2-24 $$C = \frac{\varepsilon_0}{2M''_{max}}$$

The equation is based on having an ideal capacitor. Therefore, values for the capacitance derived from the modulus are approximations, but sufficient to identify the type of process. Grain boundary capacitances are in the range of 10^{-11} to 10^{-8} F, bulk capacitances are in the range of 10^{-12} F.[32]

Analogous to the conductivity, the modulus can be used to determine the activation energy of a process. The peak maxima shown in the M'' spectra occur at certain frequencies ν_M, which are in the same order of magnitudes as the hopping frequencies ν_{hop} of the respective process. Therefore, the frequency ν_{hop}, which is related to the activation energy of the process via the Arrhenius law

2-25 $$\nu_{hop} = \nu_0 \exp\left(-\frac{E_a}{k_B T}\right)$$

can be substituted with ν_M in an approximation. By plotting the logarithm of ν_M against the inverse temperature, once again an Arrhenius plot is formed that allows the determination of E_a for a process.

2.3.2.4 *Impedance of an electrical circuit and the Nyquist plot*

Information for this chapter was taken from the book `Impedance Spectroscopy Theory, Experiment, and Applications´ by Barsoukov and Macdonald[33], unless stated otherwise.

The impedance of an electrical circuit depends on resistive, capacitive and inductive elements. For solid ionic conductors we do not expect induction and hence it is omitted from further analysis. If there are only resistive contributions to the impedance, the measured current and the applied voltage differ in their amplitudes but are in phase. This can be represented by a resistor R as electronic building block. Purely capacitive contributions, represented by the circuit element of a capacitor C, lead to a current response that is out of phase with the applied voltage. This is illustrated in Figure 10.

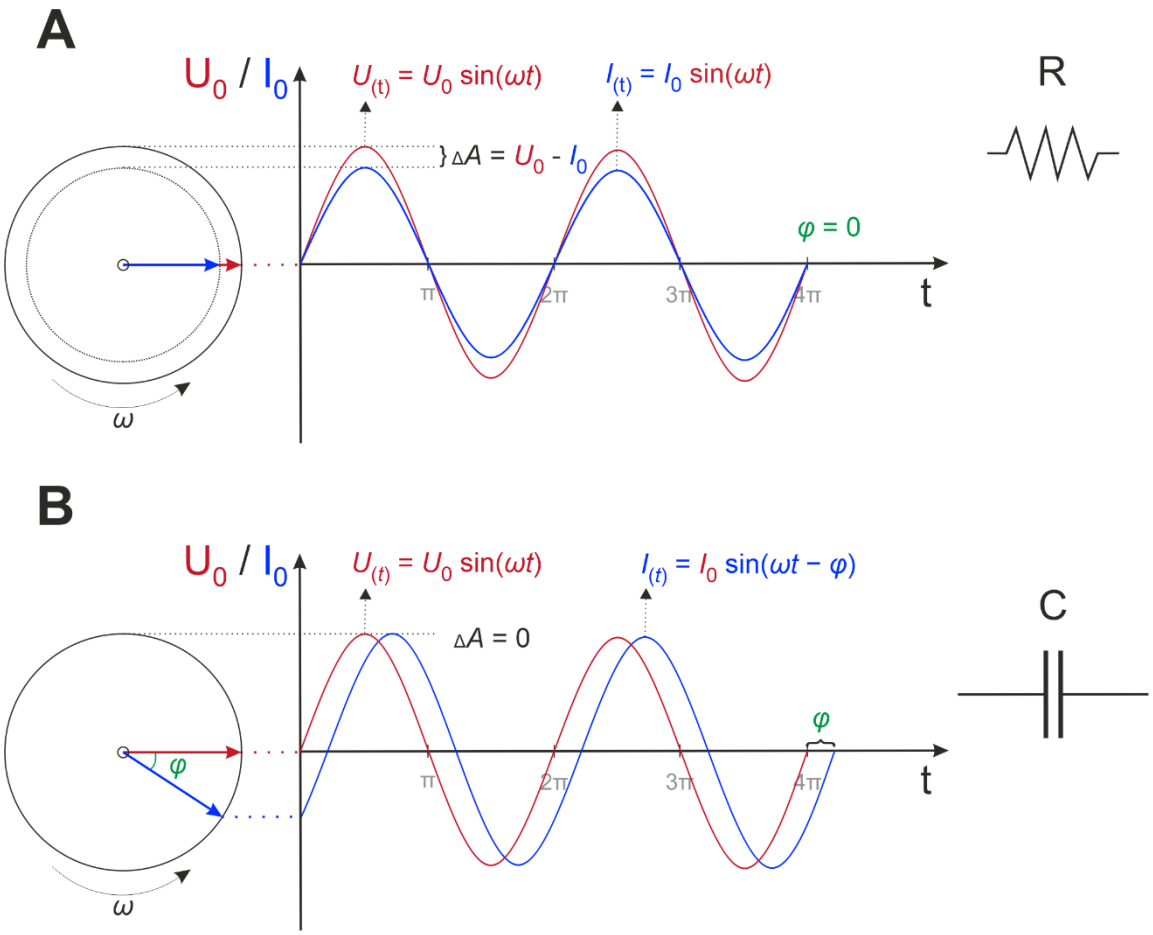

Figure 10: The impedance of a sample is a combination of resistance and capacitance. ***A*** *Purely resistive contributions, represented by the circuit element of a resistor R.* ***B*** *Purely capacitative contributions, represented by the circuit element of a capacitor C. Figure inspired by reference 27.*

The real and imaginary part of the impedance can hence be formulated as

2-26 $$Z' \equiv R$$ and 2-27 $$Z'' \equiv -\frac{1}{\omega C}$$

Resistive and capacitive contributions to the impedance can be visualized using a Nyquist plot, where the negative imaginary part of *Z*, Z´´,* is plotted against its real part *Z´*. Hereby *Z´* depends on the resistance *R* and – *Z´´* on the capacitance *C.* In case of a purely capacitive process, the corresponding Nyquist plot shows a straight line parallel to the y-axis (Figure 11 A), while a purely resistive response yields a straight line parallel to the x-axis (Figure 11 B). If both resistance and capacitance contribute to the current response of a process, the Nyquist plot depicts a semi-circle. One model to explain this behaviour is considering a resistor R and a capacitor C arranged in parallel. (Figure 11 C). The complex impedance of this model can be formulated as

2-28 $$Z^* = \frac{R}{\frac{1}{R} + j\omega RC}$$

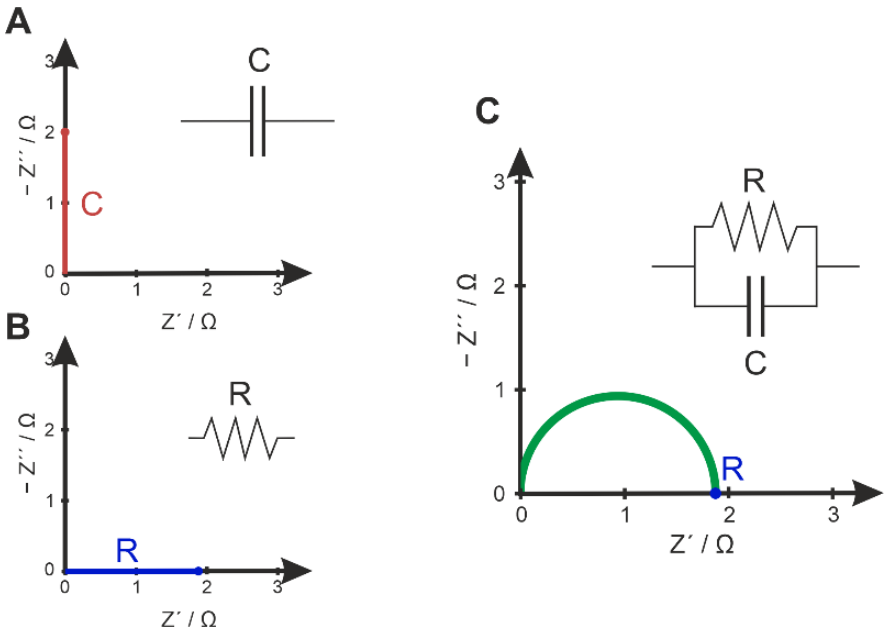

*Figure 11: Nyquist plots of different electronic building blocks. **A** The plot for a capacitor shows a straight line parallel to the y-axis. **B** The plot of a resistor shows a line parallel to the x-axis. **C** If these two elements are combined in parallel, the plot shows a semi-circle. Figure inspired by reference 27.*

At very high frequencies, the impedance of the capacitor is close to 0. The current is going through the capacitor (choosing the way of least opposition), hence the resistor does not influence the impedance and Z' in the Nyquist plot is close to 0. For the other extreme case (ω = 0), the response signal is similar to the one of DC, which cannot pass the capacitor. Consequently, the total current flows through the resistor *R* and we arrive at the maximum of the resistance. Within the intermediate frequency range, starting at ω close to zero, the capacitive contributions increase towards higher frequencies. The flow is split between *R* and *C*, as the latter is increasingly easier to pass through. At some point, the contributions of resistance and capacitance are identical, and the current is "split" in half. In the Nyquist plot the semi-circle reaches its peak, at which we have the relation

2-29 $$RC\omega = 1$$

At high frequencies, all current passes through the capacitor, bypassing the resistor. As the capacitance is proportional to 1/ω, it goes to 0 at very high ω.

To derive values for individual contributions of a diffusion process from the impedance data, it is possible to simulate the process by creating an equivalent circuit out of electronic building blocks. Elements like resistors and capacitors are connected in a way that the Nyquist plot of the equivalent circuit fits the Nyquist plot of the sample.

A resistor and a capacitor arranged in parallel, as described in the previous model, can be used to simulate each individual process in the material. A singular capacitor can model the electrode polarization. Building blocks for several diffusion processes and the electrode polarization can then be connected in series to give the complete Nyquist plot for the constructed circuit and compare it to the measured one. Via a fitting program, it is possible to obtained exact values for, in the described case, the resistance *R* and capacitance *C*.

The assumption of an ideal capacitor C is only valid in the case of electrodes with a microscopically flat surface are used. Most impedance setups do not provide such specific electrodes and therefore the impedance spectra will differ from an equivalent circuit with an ideal capacitor. To take this into account, the ideal capacitor can be substituted with a constant-phase element (CPE). This element introduces an additional resistive effect. As

illustrated in Figure 12, the use of a CPE building block results in a "tilt to the right" of the signal in the Nyquist plot by a certain angle θ. For a purely capacitive influence on the impedance this means tilting the straight line. In case of both reactant and resistant influences, represented by a resistor and a CPE arranged in parallel (ZARC element), the semicircle is depressed. The angle θ is related to an ideal capacitor via the equation

2-30 $$\theta = 90° \, (1 - n)$$

This means that the impedance of the CPE (Z_{CPE}) now depends on a capacitance Y_0 and a factor *n,* defining the deviation from an ideal capacitor, for which *n* would be 1. It can be written as

2-31 $$Z_{CPE} = \frac{1}{Y_0 \, (j\omega)^n}$$

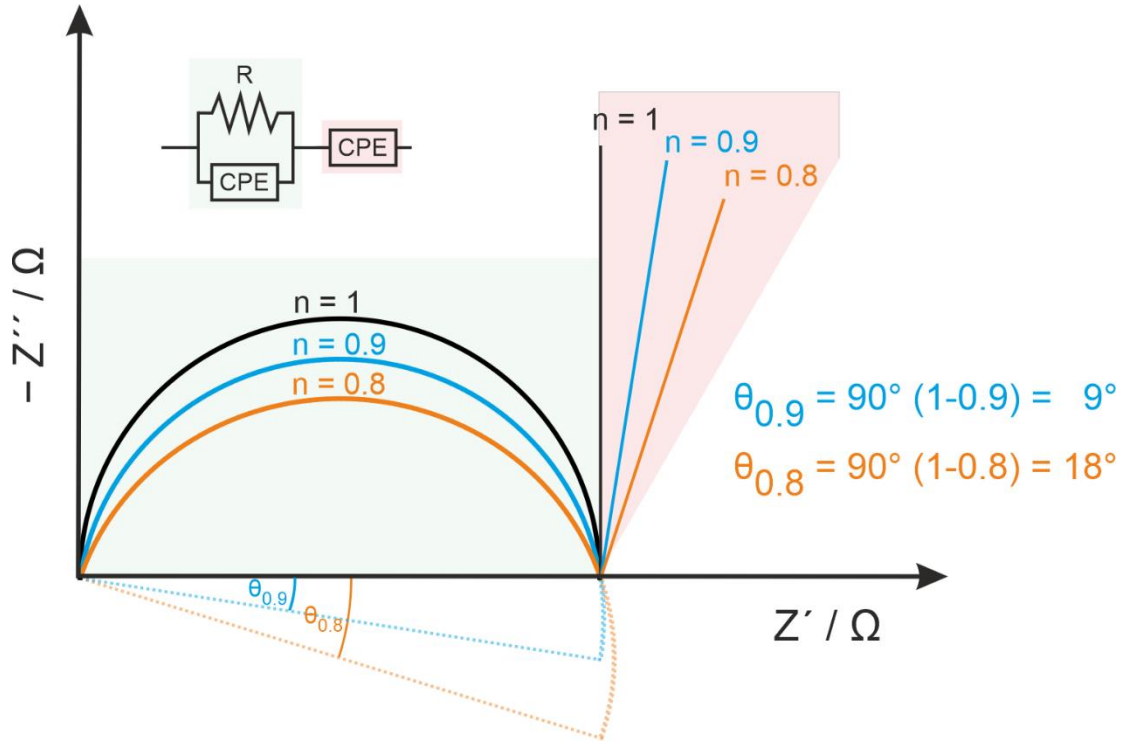

Figure 12: The constant phase element (CPE) adds a component of resistance to the capacitor. The factor n discloses how close the capacitor is to an ideal one, with n = 1 representing the perfect case. When n decreases, the straight line of a capacitor (red area) tilts to the right as there is additional resistance. In the case of a ZARC-element (green area), the semi-circle is also tilted, leading to its flattening in the Nyquist plot. Figure inspired by reference 27.

2.3.3 Solid-state nuclear magnetic resonance measurements

Solid-state nuclear magnetic resonance (NMR) spectroscopy is a method used for analysing structure of and dynamics within a sample, using the magnetic properties of nuclei inside the material. When nuclei with a magnetic moment different from zero (e.g. ^{7}Li in our case) is placed in an external magnetic field B_0, they align themselves establishing an equilibrium distribution of spin populations. When exposed to an external perturbation in the form of radio frequency pulse, this equilibrium is disturbed. The resulting changes in the magnetic field induce an electrical signal, which can be detected via inductive coupling. After the pulse is switched off, the nuclei return to their equilibrium state (relaxation). The magnitude of the recorded signal as well as the time required for relaxation provides information about the nuclei and their local electromagnetic environment.[21]

NMR relaxation methods are used to investigate dynamic properties of materials by monitoring the net magnetization over time, allowing the extraction of relaxation times. In so-called spin-lattice relaxation measurements, relaxation occurs through energy exchange between the nuclear spins and their surrounding environment (the lattice). The according relaxation time is denoted as T_1. An energy transfer from the spin to another one is defined as spin-spin relaxation, with the relaxation time T_2. In the case of $T_{1\rho}$ measurements, the spin is "locked", using an additional magnetic field B_1. Its relaxation time lies between T_1 und T_2 and depends on the applied locking frequency. The inverse relaxation times (T_x^{-1} with (x=1,2); relaxation rates) are then used to estimate the jump rates of the observed processes (illustrated in Figure 13).[34] A shorter relaxation time means that an atom performs more successful jumps during which their kinetic energy is transferred to the environment. In contrast to the long-range transport processes analysed by DC conductivity measurement, NMR relaxation methods only detect motion in the kHz to GHz range and are therefore more sensitive to both localized jump processes and long range transport, depending on temperature.[21,35]

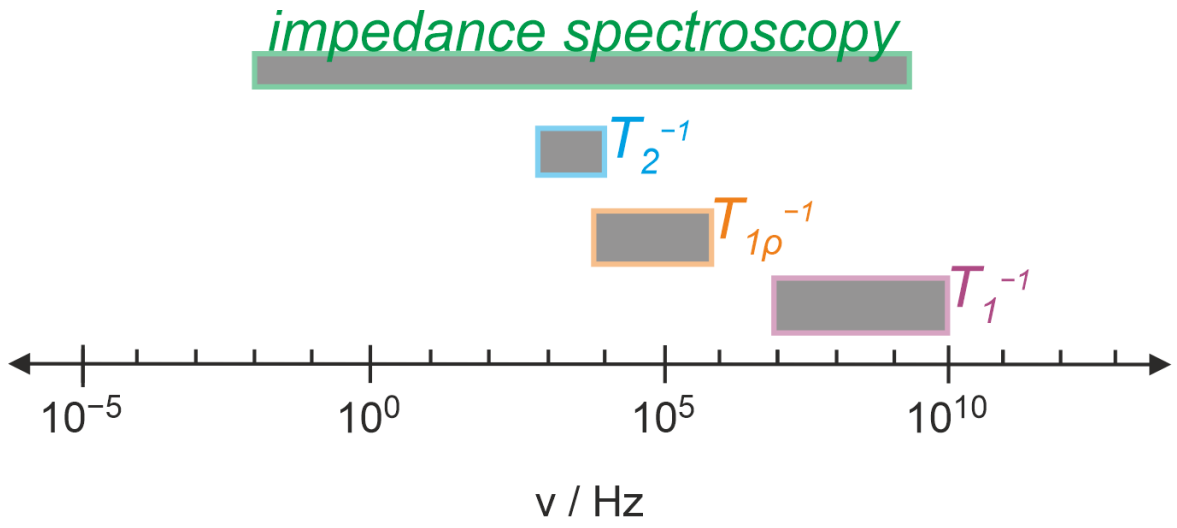

Figure 13: NMR relaxation methods can detect jumps in kHz and GHz range, compared to a wider frequency range probed by impedance spectroscopy measurement in this thesis. Their relaxation rates T_1^{-1}, $T_{1\rho}^{-1}$ and T_2^{-1} are in the frequency range of the jump rate of an ion in the material. Figure inspired by reference 36.

When the temperature-dependence of the relaxation rates is presented in an Arrhenius plot, it is possible to deduce activation energies for the jump processes by using a certain fit function. The relaxation rate of a process increases with rising temperature up to a certain maximum (rate peak, at the temperature where the jump rate is in the order of the correlation rate). After that it declines when the temperature is further increased. This divides the plot into two areas, namely, the high-temperature and low-temperature flank.[35]

3 Experimental part

All experimental work has been conducted by Sarah Lunghammer, a former co-worker at the Institute for Chemistry and Technology of Materials (ICTM). A more detailed description can be found in her master thesis.[20]

3.1 Synthesis

$Li_2Ti_3O_7$ was synthesised according to the solid-phase synthesis described by De Dompablo *et al.*[14,15], following the stochiometric equation

$$3\,TiO_2 + Li_2CO_3 \rightarrow Li_2Ti_3O_7 + CO_2$$

The educts TiO_2 and Li_2CO_3 were mixed in a Fritsch Pulverisette 7 premium line planetary mill (using a 45 ml ZrO_2 beaker and 180 ZrO_2 balls of 5 mm diameter) in the stoichiometric ratio 3:1 and milled at 500 rpm for 13 hours. Afterwards, the obtained powder was heated up to 1000 °C at a rate of 7 °C per minute. After holding the temperature for two hours, the product was quenched on air down to room temperature (RT; 20 °C), in order to preserve the ramsdellite structure. XRPD was used to confirm the ramsdellite structure and to determine the purity of the sample.

3.2 Impedance measurement

The synthesized powder was pressed into pellets with a diameter of 5 mm and a thickness of about 1.5 mm, by applying uniaxial pressure of 10 kN for 15 minutes. The samples were then sputtered with a gold layer (100 nm on each side) under argon atmosphere, using a Leica EM SCDO50 sputter coater. Impedance measurements were conducted using a Novocontrol Concept 80 broadband dielectric spectrometer. For measurements in the conventional

(standard) frequency range from 10 mHz to 10 MHz, the sample was placed inside a Novocontrol active ZGS sample cell. Complex impedance data were recorded using an Alpha A frequency analyser from Novocontrol. In order to increase the frequency further, measurements required an Agilent E4991 A high-frequency analyser and the use of a specially designed high-frequency cell as sample holder (both from Novocontrol). With this second setup, impedance data in a frequency range from 1 MHz to 3 GHz were collected.

The temperature inside the sample chamber was controlled via a QUATRO Cryosystem from Novocontrol, regulated by freshly evaporated N_2 - stream. The temperature program is shown in Figure 14: All temperature steps, whether heating or cooling, were in 20 °C increments. For measurements in the standard frequency range, the sample was heated up from RT to 100 °C, then cooled down to −120 °C and subsequently heated up to 200 °C. After confirming that no changes occurred during the measurement due to thermal treatment - by comparing data from the initial heating and cooling runs - the data from the last heating sequence were used for the analysis, covering a temperature range from 153 to 473 K. Afterwards, the sample was cooled down to RT. The temperature program for the high-frequency measurements was identical, except that the cooling steps only reached down to −100 °C instead of −120 °C, resulting in an analysed temperature range from 173 to 473 K.

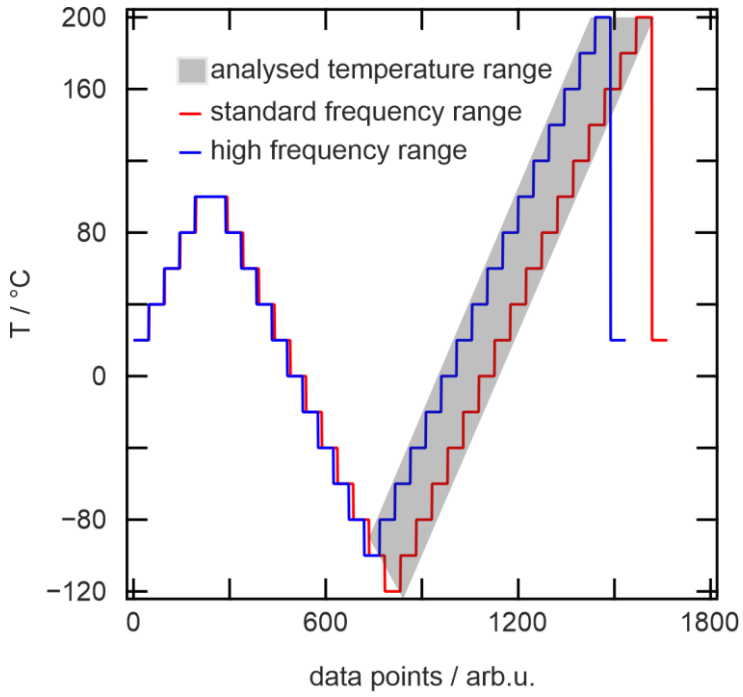

Figure 14: Temperature program for the impedance measurements of $Li_2Ti_3O_7$ at standard frequencies (red) and high frequencies (blue). Data from the second heating sequence (grey area) were used for the analysis of the material after ruling out any changes during initial heating and cooling.

4 Results and Discussion

All raw data on impedance and NMR we present and analyze in this thesis were originally collected by Sarah Lunghammer during her work as master and PhD student and subsequently analyzed extensively here. XRPD measurements as well as their analysis were conducted by B. Bitschnau, F. Mautner and their respective groups from the Institute of Physical and Theoretical Chemistry at the TU Graz.

4.1 XRPD

The successful synthesis of $Li_2Ti_3O_7$ was confirmed by XRPD measurements. A reference pattern from a database (ICSD 169864) was used to determine the structural purity of the sample, which was found to be 100%, ruling out potential LTO side phases (Figure 15). The ramsdellite structure is additionally confirmed by comparing it with data from literature. The XRPD diffractogram shows all the reflections related to ramsdellite-structured $Li_2Ti_3O_7$.[37]

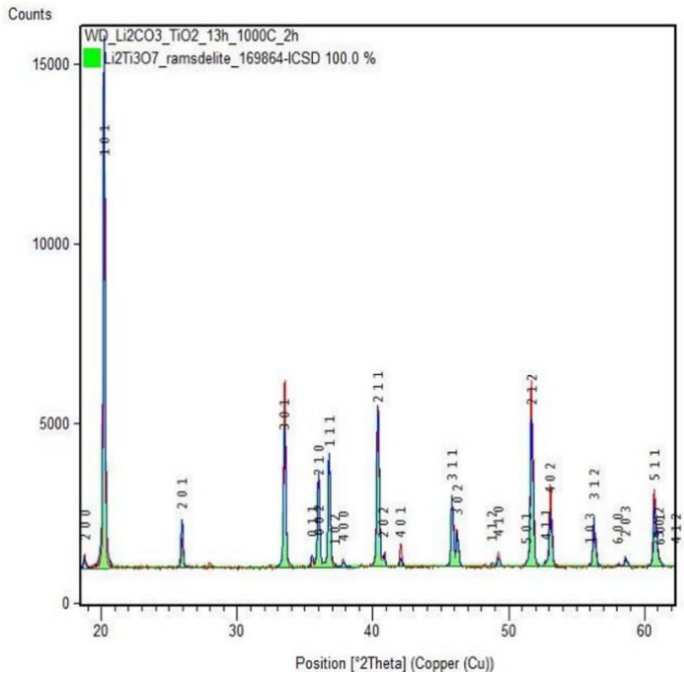

Figure 15: XRPD diffractogram of the sample. The comparison with a databank confirms the complete transformation of the educts into the desired ramsdellite $Li_2Ti_3O_7$. Image taken from the master thesis of Lunghammer, reference 20.

4.2 Impedance spectroscopy

Impedance measurements were conducted at conventional frequencies (10^{-2} to 10^{7} Hz) and high frequencies (10^{6} to 10^{9} Hz). Throughout this thesis, measurements in the conventional frequency range will be referred to as low-frequency (LF) measurements with respect to those conducted at higher frequencies (HF). For all following spectra, the results of both measurements are combined in one plot. Hereby, data points from LF measurements are depicted as circles, those from HF measurements as triangles, unless stated otherwise.

4.2.1 Conductivity

By plotting the logarithm of the real part σ' of the complex conductivity at different temperatures against the frequency ν of the applied alternating voltage, the conductivity isotherms of the material can be depicted. Figure 16 shows the conductivity isotherms of $Li_2Ti_3O_7$. The conductivity increases with temperature and applied AC frequency.

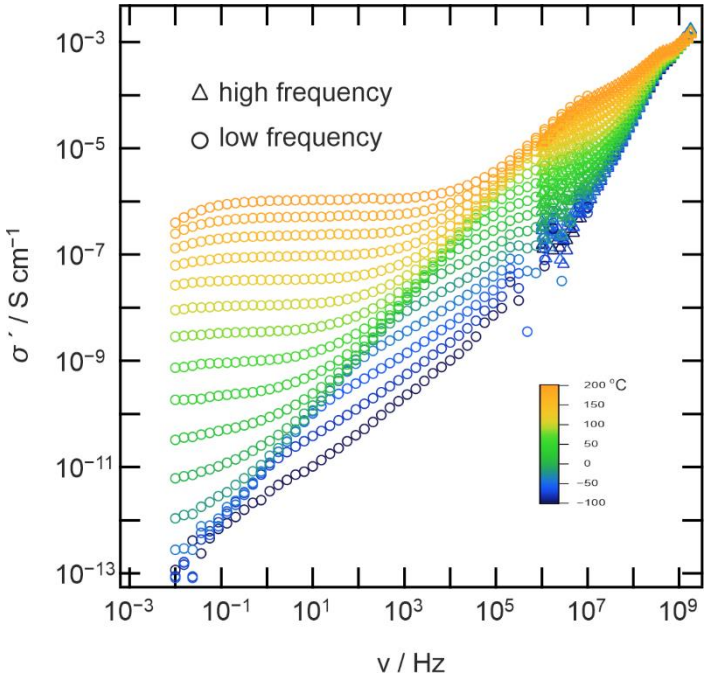

Figure 16: Conductivity isotherms of $Li_2Ti_3O_7$ in a temperature range from −100 to 200 °C, in steps of 20 °C. The plot combines spectra obtained from both low-frequency (LF, circles) and high-frequency (HF, triangles) measurements.

As depicted in Figure 17, the conductivity spectra of $Li_2Ti_3O_7$ indicate that three ion diffusion processes contribute to the overall conductivity (from now on referred to as A, B and C). Each process is connected to a so-called DC plateau of the isotherm, where the conductivity (σ_{DC}) is frequency-independent because it originates from successful long-range transport of Li^+ ions. Towards higher frequencies, local jump processes start to contribute to the conductivity, leading to a transition into a dispersive regime. The decrease in conductivity towards low frequencies at high temperatures is due to charge carriers accumulating at the electrodes (electrode polarization). These conductivity regimes are discussed in more detail in the theoretical part on conductivity isotherms (section 2.3.2.1). To determine the frequency of the DC plateaus, the dissipation factor tan(δ), can be used. If the imaginary part Z'' of the complex impedance approaches 0, as it is the case for frequency-independent conductivity plateaus, tan(δ) goes towards infinity. Therefore, the frequency at the maximum of tan(δ) equals that of σ_{DC}. For process A, DC plateaus (σ_{DC}) occur in a frequency range from 10 mHz to 0.1 kHz. The DC plateaus of process B lie between frequencies of 10 Hz and 10 MHz. These plateaus are not distinctly visible in the conductivity spectra in Figure 17 because of an overlapping capacitive contribution, but they can be localized via the maximum of tan(δ). The third process (C) exhibits DC plateaus at frequencies around 0.4 GHz.

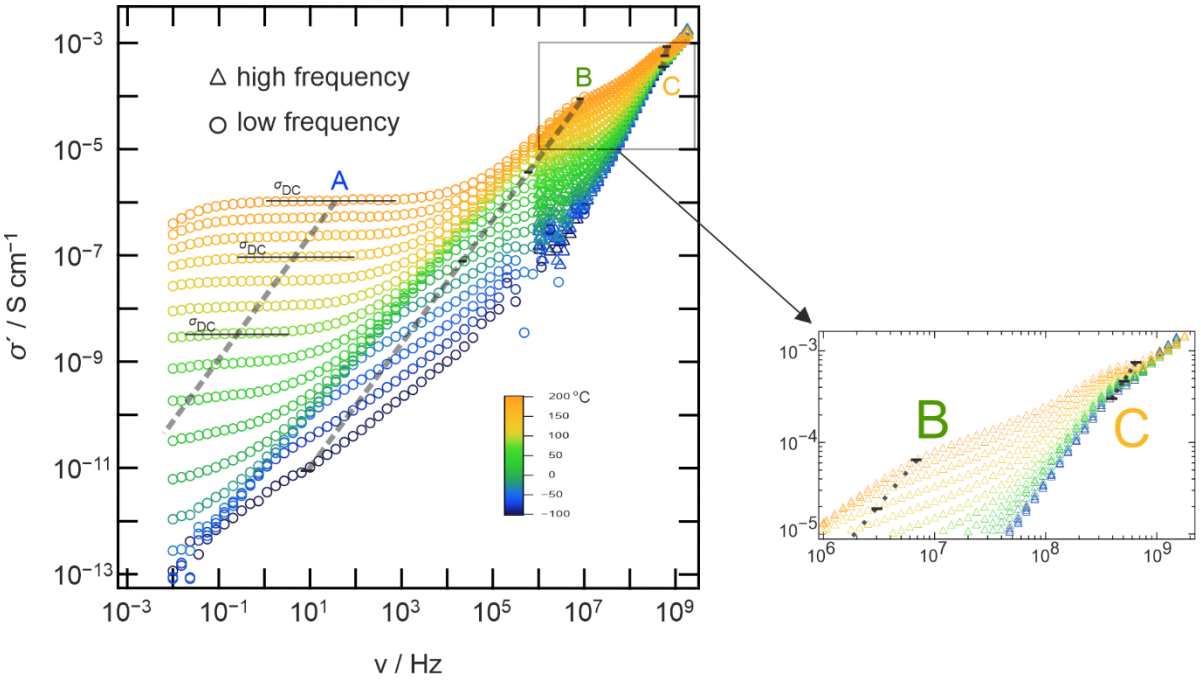

Figure 17: Conductivity isotherms showing the DC plateaus of the three distinct processes (A, B and C), indicated by solid black lines. The DC plateaus shift towards higher frequencies with rising temperature (dashed lines). The inset shows a magnification of the DC plateaus of process B and C.

To determine the dimensionality of $Li_2Ti_3O_7$, we use the empirical model of Jonscher, described in section 2.3.2.2. The DC plateau and the dispersive regime were fitted according to equation 2-21. As depicted in Figure 18, in three different areas of the plot have been chosen for the fits. For process A, fits were applied for temperatures from 80 to 200 °C in the LF region. DC plateaus for process B were fitted twice, one time in the LF region for temperatures from −100 to −20 °C and one time in the HF region for temperatures between 140 and 200 °C. The obtained values for *n* from the respective fits are therefore analysed separately.

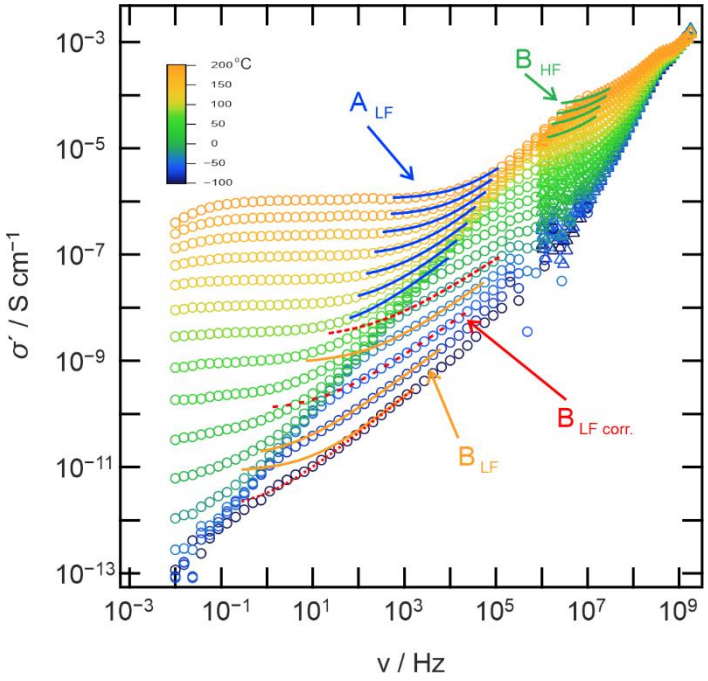

Figure 18: Jonscher fits in different areas of the conductivity spectra. In the low frequency area have one fit for the first process A (blue) and one for process B at low temperatures (red), while for high temperatures we have fitted in the high frequency area for B (green). In addition, we performed a corrected Jonscher fit for B in the LF area (orange).

The model of Jonscher[29] suggests that the dimensionality of a diffusion process is connected to the power law exponent obtained from the fit. In the case of the fits for process A, power law exponents from 0.67 to 0.75 were obtained. This would define A as a 3D diffusion process, which is expected for grain boundary diffusion. Fits for process B at LF yield values for *n* between 0.62 and 0.69. Though they are smaller than those for process A, the dimensionality of diffusion is still considered 3D according to the model. Fits for process B at HF yield power law exponents even larger than those for process A, ranging from 0.74 to 0.84. Regarding

these fits, Jonscher`s universal power law would predict a 3D diffusion process, contradicting the assumption of $Li_2Ti_3O_7$ being a quasi-1D ion conductor. The reason for this deviation could lie in the limitations of the applied fit as well as in the purely empirical nature of the Jonscher model. Moreover, the plateaus of process B are — as already mentioned above — superimposed by an additional capacitive effect. This is particularly apparent at low frequencies, where the exact position of the DC plateaus cannot be determined by considering the conductivity isotherms alone. To take the superposition into consideration, the resistance *R* of the bulk process has been approximated using Nyquist plots (theoretical background can be found in section 2.3.2.4). The exact method is described in the appendix. With this approximation, corrected Jonscher fits (Jonscher fit_{corr}) are obtained for process B at LF ($B_{LFcorr.}$; as depicted in Figure 18). The related power law exponents n_{corr} range from 0.69 to 0.55. They are generally smaller than those obtained from the initial Jonscher fits, in some cases fulfilling the requirements of the universal power law for 2D, but not for the anticipated quasi-1D diffusion with an exponent smaller than 0.4.

In the case of process C it is not possible to perform a Jonscher fit, as the obtained values for σ_{DC} would be lower than the conductivities of the DC plateaus in the spectra. Possible fits correctly depicting the conductivity isotherms would have had exponents larger than 1, which does not comply with Jonschers model.

4.2.2 Modulus

Modulus spectra, that is, when the imaginary part M'' of the complex modulus is plotted against frequency, are used to confirm the three diffusion processes derived from analysing the conductivity isotherms. In addition, it provides information on the type of diffusion process, because M'' at the peak maxima is inversely proportional to the capacitance. As first approximation, peaks with a magnitude of 10^{-2} arbitrary units (arb.u.) are attributed to bulk processes in the material, while those between 10^{-3} to 10^{-5} arb.u. are assigned to grain boundary (g.b) processes. Subsequently, specific values for the capacitance of each process can be derived from the peaks in the M'' spectrum via equation 2-24. For the analysis of the modulus, it must be noted that the values for M'' obtained from the HF measurements are larger than those from LF measurements. By plotting M'' for LF and HF on opposite axes against the frequency, the axes can be adjusted so that the data points form coherent spectra as it is shown in Figure 19. A direct comparison reveals that values gathered from HF measurements are approximately 1.4 times larger than those from LF, which might be related to the different sample geometries as well as the measurements itself. As the differences do not have a significant impact on the results in terms of process identification, it has been decided to use the M'' values from the LF measurements to discuss the results, though there is no reason to prefer one measurement over the other.

Modulus spectra of $Li_2Ti_3O_7$ exhibit three distinct peaks for each temperature, as is shown in Figure 19. One peak at low frequencies can be related to the first DC plateau (process A) of the conductivity isotherms and has an amplitude of about $2 \cdot 10^{-3}$, which is within the range of a grain boundary process. The second peak at higher frequencies shows amplitudes ranging from $7 \cdot 10^{-3}$ to $12 \cdot 10^{-3}$ arb.u., hence they lie between the typical values observed for bulk and grain boundary processes. The amplitudes hereby increase with higher temperature. The third peak occurs within a constant frequency range of 2.5 to $3.8 \cdot 10^{8}$ Hz, similar to the respective DC plateaus of the conductivity isotherms. The frequency of the peak maximum is therefore seemingly temperature-independent. Its intensities are almost constant up to 0 °C and then increase rapidly with temperature, approaching the amplitudes of a bulk process.

Interestingly, at −100 °C a shoulder in the peak of process B can be seen, which is indicated in a red circle in Figure 19. The peak disappears at higher temperatures and is considered an artefact of the measurement.

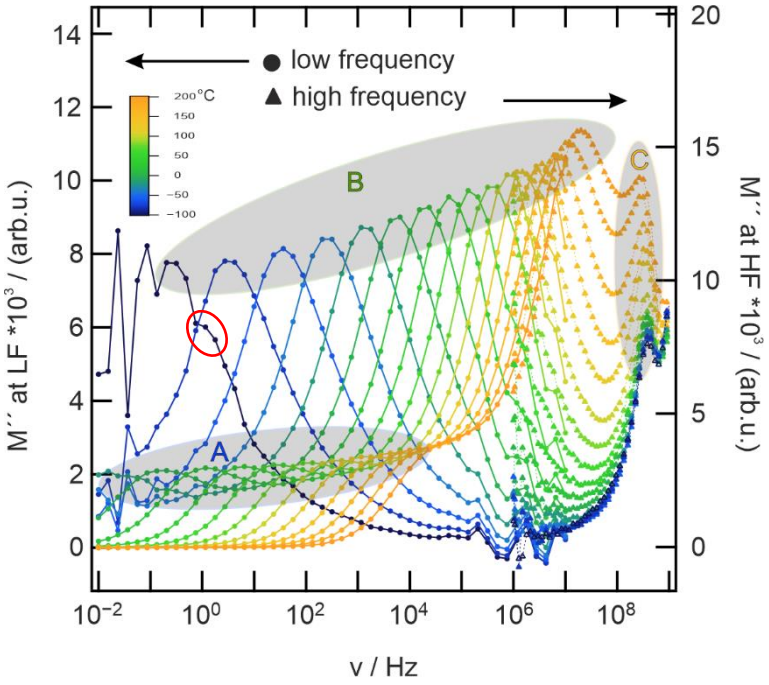

Figure 19: The imaginary part M´´ of the complex modulus, plotted against the frequency. The spectra show three peaks (A,B and C) for each temperature. In addition to the three main peaks, a small shoulder around a frequency of 1 Hz at -100 °C (red circle) is detected, which vanishes at higher temperatures. The plot contains the values from the LF mesaurements on the left y-axis and the ones for the HF measurements on the right y-axis.

Taking a closer look into the temperature-dependence of the peaks, the spectra for 0, 100 and 200 °C are outlined in Figure 20. The g.b. peak (process A) is shifting towards higher frequencies when the temperature increases. This leads to an overlap with the peak representing the bulk processes. The intensity of the latter does also increase when the material is heated up, and its maximum shifts towards higher frequencies as well, but not as significantly as the grain boundary peak. The intensity of the third (process C) peak remains nearly constant below 0 °C (as already seen in Figure 19), but increases noticeably towards higher temperatures - from $6.1 \cdot 10^{-3}$ arb.u. at 0 °C, over $6.8 \cdot 10^{-3}$ at 100 °C to $10.2 \cdot 10^{-3}$ arb.u. at 200 °C. An explanation for this strong change in intensity could be the overlap with peaks from the bulk process B (see Figure 20). In that case, one would assume that the intensity has an initial value of around $6 \cdot 10^{-3}$ arb.u., derived from peaks at lower temperatures where there is no overlap. While the peaks of A and B shift toward higher frequencies with rising temperature, peaks of process C appear at an almost constant frequency. This frequency-independence sets C apart from the other two processes. It could point to lattice vibrations within the material or an artefact of the HF measurement.

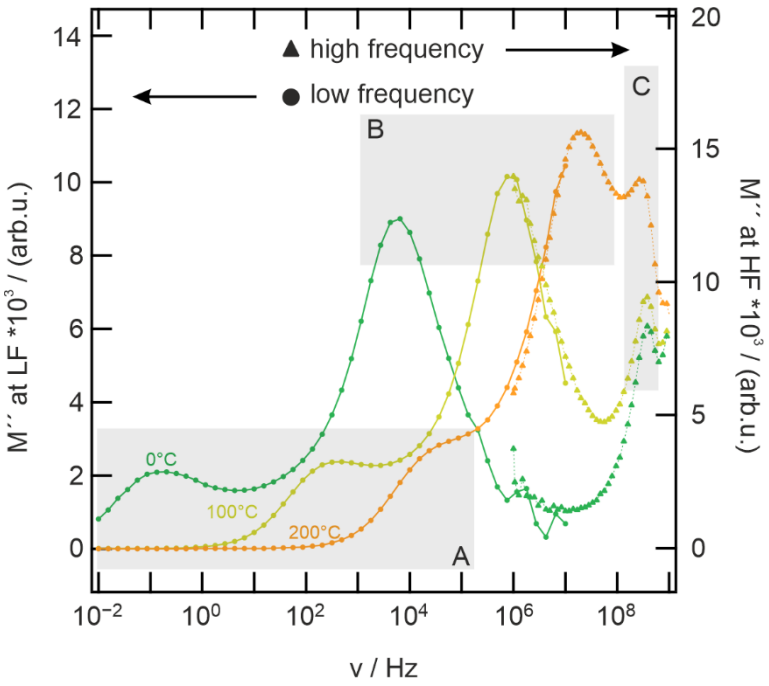

Figure 20: Imaginary part of the complex modulus (M´´) for 0, 100 and 200 °C plotted against frequency, depicting the temperature-dependence of the peaks for all three processes A, B and C. Data from the LF measurments refere to the right y-axis, data from the HF measurements to the left one.

For the first peak, representing process A, capacitances are in the range of 20 to 27 pF (24 pF at 100 °C), which is at the lower end of the typical range for grain boundary processes (10^{-11} to 10^{-8} F). Capacitances of the second peak (process B) are decreasing from 7 to 6 pF with rising temperature (6 pF at 100 °C), confirming the assignment to a bulk process. For process C, capacitances are in a similar range, from 7 to 10 pF (8 pF at 100 °C). The capacitances of the highest temperatures (140 to 200 °C) for the processes B and C are excluded, as the overlapping of their peaks in the modulus spectra is expected to cause an underestimation of the capacitance. It should be noted that all peaks of the modulus for process C appear at high frequencies. Therefore, the capacitances are calculated from the exact HF values and then multiplied with 1.4. Although this is an approximation, it is considered sufficient to characterize the process.

4.2.3 Nyquist plot and equivalent circuits

Because equation 2-24 is based on the use of an ideal capacitor, values for the capacitance of a process derived from modulus spectra are an approximation. To get more precise information on the capacitances, Nyquist plots of $Li_2Ti_3O_7$ were simulated using an equivalent circuit, following the model presented in section 2.3.2.4:

Nyquist plots are formed by plotting the negative imaginary part of the complex impedance ($-Z''$) against its real part Z'. They provide information about the resistance R and the capacitance C within the sample, as well as on the interfaces. For $Li_2Ti_3O_7$, the Nyquist plot, which is illustrated exemplary for 100 °C in Figure 21, exhibits two overlapping semi-circles, each one representing an ion diffusion process. At low frequencies, the electrode polarization leads to a straight, ascending line.

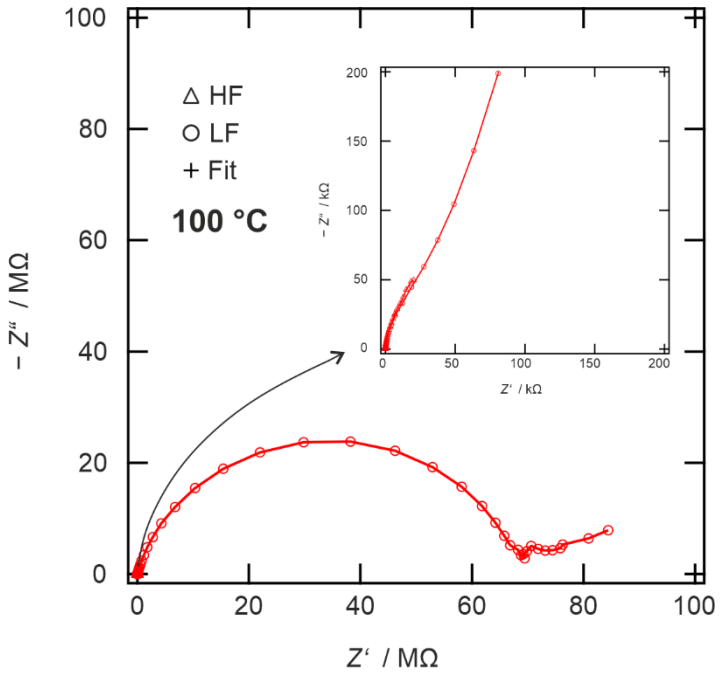

Figure 21: Nyquist plot of $Li_2Ti_3O_7$ at 100 °C shows two overlapping semi-circles. A smaller one at higher frequencies (on the left side of the plot, visible in the zoomed-in region) is mostly superimposed by a larger one. Each semicircle stems from an individual ion diffusion process. At lower frequencies (right side of the plot), the polarization of the electrodes used for the measurement causes a straight line.

The equivalent circuit used for the fit of the Nyquist plot consists of two ZARC elements using CPEs as capacitors to simulate both resistive and capacitive behaviour of the two processes found in previous analyses. After the elements for the bulk (R1; CPE1) and grain boundary (R2; CPE2) ion diffusion in the material, an additional CPE is introduced in series to represent the electrode polarization (Figure 22).

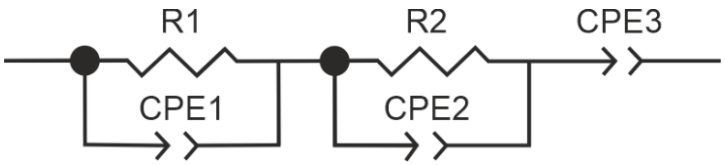

Figure 22: The equivalent circuit for two diffusion processes (1 and 2) and the electrode polarization (3).

Attempts to find an electronic building block for simulate the third process C were not successful, as the measurements do not provide enough data points in the HF region to identify a potential third semi-circle. Fits were performed using the program Z-View.

At 100 °C, the fit of the Nyquist plot yields capacitances of 86 pF and 9 pF to the grain boundary and bulk process, respectively, as depicted in Figure 23. These values are in agreement with results presented in the dissertation of Heine[38], with capacitances of 70 pF and 7 pF derived from the permittivity. Moreover, the fit yields a capacitance of 0.28 µF for the electrode polarization, which is lower than that observed in the dissertation, 7 µF. The line representing electrode polarization is bent in the plot, therefore, only the initial slope from the end of the semi-circle was fitted. The lower frequency limit of the measurement could provide an explanation for this behaviour: When considering the conductivity spectra in Figure 16 (page 28), it can be noted that the measured frequency range does not include a visible regime of the electrode polarization at 100 °C. The resistance of the bulk process is 27 kΩ, the one of the g.b. process 69 MΩ. The latter is three orders of magnitudes larger than values in the dissertation, which could be related to variations in the synthesis. For instance, reduction in particle size can significantly increase the resistance, as reported by Gadermaier *et al.*[39]

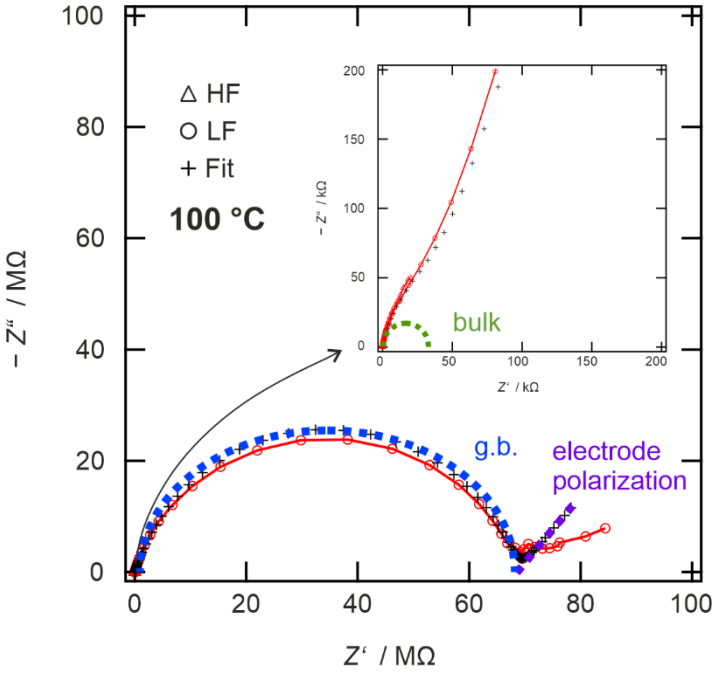

Figure 23: Fit of the Nyquist plot at 100 °C to identify two diffusion processes and the electrode polarization. Tthe plot depicts a bulk (green) and grain boundary process (blue) as well as the electrode polarization (purple) at low frequencies.

At 200 °C, the Nyquist plot shows two overlapping semi-circles as well (Figure 24). The resistance for the g. b. process is 7 MΩ, compared to 1.5 kΩ for the bulk one. A decrease in resistance with rising temperature is expected, as there is more thermal energy available for jump processes and hence diffusion of lithium ions. While a capacitance of 9 pF from the fit for the bulk process is identical to the one at 100 °C, the capacitance obtained for the grain boundary process is about twice as high (184 instead of 86 pF). This is surprising, as the capacitive values derived from the modulus show a decrease with rising temperature. A possible reason for the deviation might be the overlap of LF and HF data points, which influences the fit. At 200 °C, a larger part of the grain boundary process lies within this overlapping area.

The capacitance of the CPE element attributed to the electrode polarization at 200 °C is 6 µF, which is closer to the value from Heine of 7 µF (in comparison to 0.28 µF at 100 °C). This is expected, because a rise in temperature shifts the effect of the electrode polarization towards higher frequencies. At 200 °C, the process may already be fully captured in the Nyquist plot.

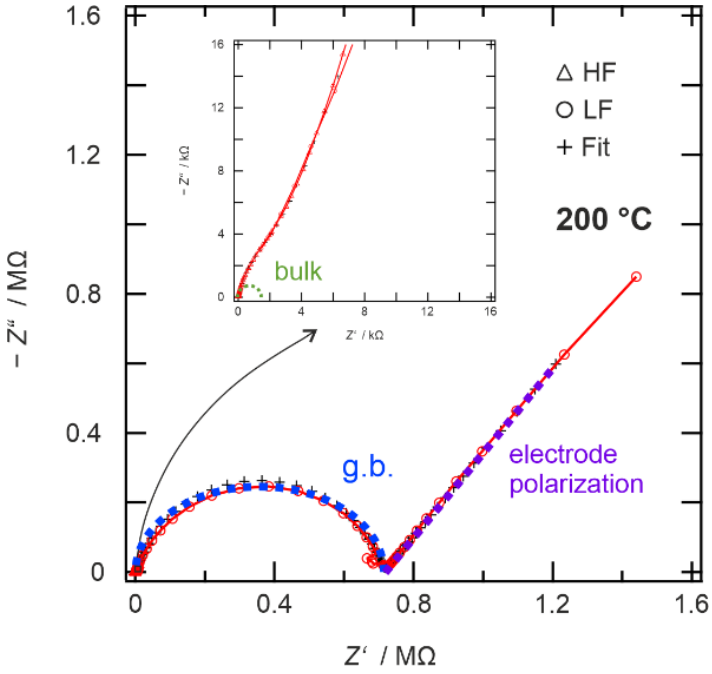

Figure 24: Fit of the Nyquist plot at 200 °C, showing the same two diffusion processes as for the one at 100 °C. As the influence of the electrode polarization increases with higher temperature, the straight line representing it is more pronounced.

The factor *n* of the CPE elements in the fit, which denotes their proximity to an ideal capacitor, is similar for both 100 and 200 °C. It yields about 0.99 for bulk, 0.80 for grain boundary and 0.56 for the electrode polarization. This is in accordance with the theory that *n* depends on the electrodes used in the measurement and is therefore temperature-independent. In case of the electrode polarization, the factor is very close to the theoretical value of 0.5.[40]

4.2.4 Activation energies

The activation energies of processes are determined in three different ways, via the DC conductivities, the peak positions from the modulus spectra and the crossover frequency (ν_c) derived from the Jonscher fits. In all three cases, the Arrhenius plot allows linear fits of the data points. The slopes of these fits provide the activation energies (E_a) of the individual processes as described in the theory part (section 2.3.2.1). The Arrhenius plot derived from the DC conductivities σ_{DC} depicts the three different processes A, B and C, as illustrated in Figure 25. The activation energies of the grain boundary and bulk process are 0.72 and 0.49 eV, respectively. Heine deduced similar E_a for $Li_2Ti_3O_7$ in her dissertation, namely 0.55 and 0.48 eV. Boyce and Mikkelsen found the activation energies ranging from 0.44 to 0.47 eV when they studied single crystal $Li_2Ti_3O_7$.[41] This further confirms the characterisation of process B as bulk process. For the unidentified process C, we do get an E_a of 0.03 eV.

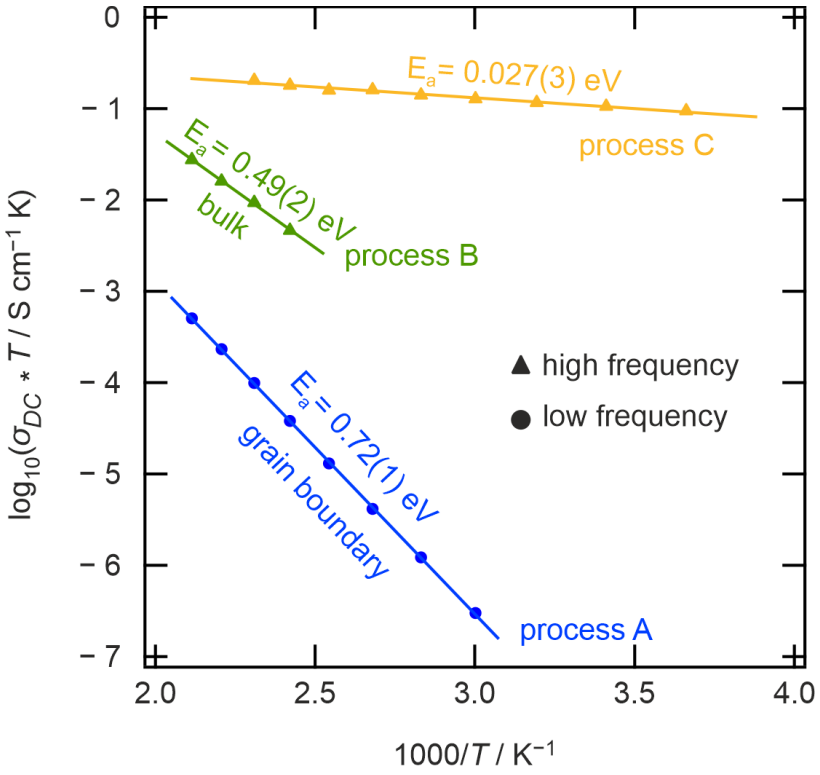

Figure 25: Arrhenius plot deduced from the conductivity plateaus σ_{DC}, yielding activation energies for the processes A, B and C (blue, green and orange respectively) by linear fits of the data points. For A, data points are obtained LF measurements (●), for B and C they came from HF measuremnts (▲).

The Arrhenius plot depicted in Figure 26 combines data points gathered from the modulus spectra and the Jonscher fits, showing the two processes A and B. Both the frequencies at the modulus peak maxima (ν_M) and crossover frequency (ν_c) are considered to be in the order of magnitude of the hopping frequency ν_{hop}, which is described in section 2.1.3. They can therefore be viewed as interchangeable for the scope of the thesis and fitted together. The fit for process A yields an activation energy of 0.67 eV, the one for process B 0.43 eV. These values are in accordance with those obtained from the Arrhenius plot of the conductivity (0.72 and 0.49 eV; see Figure 25). In general, activation energies derived from the modulus are smaller than those derived from the conductivity spectra, as the modulus reflects localized motion and does not account for the energy needed for long-range ion transport. Deviations from the linear fit are due to the discrete frequency values of the measurement, not depicting the exact maxima of *M´´* peaks, as well as the fact that ν_c is obtained from a fit and is therefore regarded as an approximation. The latter is apparent especially in the case of ν_c values at −100 °C (Figure 26; red circle), which were excluded from the fit as outliers.

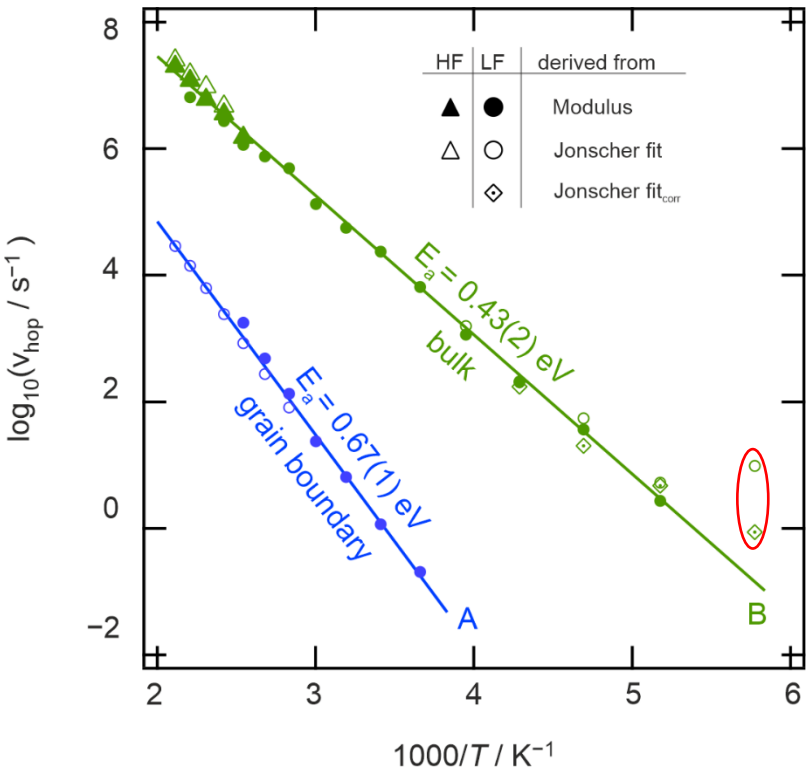

Figure 26: Arrhenius plot of the frequencies gatherd from M´´ peaks (filled symbols) and the Jonscher fits (open symbols). For the grain boundary process (blue), this includes ν_M and ν_C rates from LF measurements, while the bulk process (green) has additional values from high frequency measurement (HF) and those of a corrected Jonscher fit (Jonscher fit$_{corr}$). Frequencies derived from Jonscher fits of the bulk process at −100 °C (red circle) were not considered for the linear fit.

As already discussed above, the frequencies at which the modulus peaks and the DC plateaus occur for process C are seemingly temperature-independent. Consequently, plotting them against the inverse temperature results in a straight line of data points parallel to the x-axis with an activation energy of about zero. Therefore, the data from this process are not included in Figure 26.

In summary, we were able to identify three potential ion diffusion processes using impedance spectroscopy in a frequency range from 10 mHz to 3 GHz. The process at the lowest frequencies (10 mHz to 10 kHz) represents long-range diffusion within the material. Its peaks in the modulus spectra with intensities of about $2 \cdot 10^{-3}$ suggest a grain boundary process. From these peaks we deduced a capacitance of 24 pF at 100 °C, assuming an ideal capacitor. This is significantly lower than the capacitance deduced from the Nyquist plot fits, which gave 86 pF at 100 °C and 184 pF at 200 °C. The difference between the capacitances of the two fits is significant and might be a result of the overlap in frequency ranges of HF and LF measurements. The capacitances of both Nyquist-fits can be assigned to a grain boundary process as well. The activation energy of the process is 0.72 eV and 0.67 eV, according to the Arrhenius plots derived from conductivity and modulus spectra, respectively. The latter also includes values from the Jonscher fits of the conductivity isotherms. The second process B appears in a frequency range from 0.1 Hz to 10 MHz. The intensities of the peaks from the modulus and hence the resulting capacitance lie in the range of bulk processes (0.01 and 6 pF, respectively at 100 °C), which was confirmed by fitting the Nyquist plots at 100 °C and 200 °C, both yielding 9 pF. The activation energy of the process is 0.49 eV derived from the DC conductivity and 0.43 eV derived from the hopping frequencies. These values are in accordance with activation energies for bulk processes of $Li_2Ti_3O_7$ found in literature for both single-crystal and polycrystal samples. Jonscher fits for the process yield exponents between 0.62 and 0.69. This means that the empirical Jonscher model does not indicate a 1D ion-diffusion process.

The third process at high frequencies (around 0.38 GHz) yields DC conductivities in the range of 0.41 to 0.69 mS cm^{-1}. With values around $6 \cdot 10^{-3}$ arb.u., the peaks of the modulus spectra between the ranges assigned to grain boundary and bulk processes. At temperatures above 100 °C, the intensities of the maxima increase significantly, which is attributed to an overlap of the peaks with those from process B. The capacitance derived from the modulus is 11 pF at 100 °C (estimated based on the deviation between LF and HF values). We were not able to identify process C in the Nyquist plot. Interestingly, the frequencies of both the DC plateaus and modulus peaks appear to be temperature-independent. This may point to the process being an artefact of the measurement. Alternatively, frequency resolution of the measurements might not be high enough to detect the temperature-dependence, though this option seems less likely, as the frequencies of the modulus peaks slightly decrease at high

temperatures. While E_a can be derived from the DC conductivity (0.03 eV), another effect of the frequency-independence is that an Arrhenius plot from the hopping frequencies yield an activation energy of zero, or, in case of the mentioned frequency trend at high temperatures, even a negative one.

Electrode polarization is visible in the conductivity spectra of temperatures above 100 °C. While it can be identified using the Nyquist plot at 100 °C, the capacitance derived by the fit (0.3 µF) is about 20 times smaller than those of the fully depicted form at 200 °C (6 µF, which fully captures the electrode polarization process), as well as values found in literature.

4.3 Comparison to results from solid-state NMR

In a final step, we compare our results with data from NMR measurements on $Li_2Ti_3O_7$ conducted and analysed by Sarah Lunghammer in her master thesis.[20] While a wide variety of NMR methods was used, we focus on ^{7}Li relaxation measurements. All three methods, that is T_1, $T_{1\rho}$ and T_2, yield a single relaxation rate, implying a single jump process of Li^+ in the material. As NMR methods are more sensitive to bulk processes – due to their relative abundance in the sample compared to grain boundary diffusion –, Lunghammer concluded that the signal represents a Li^+ transport process in the bulk of the sample. Consequently, we suggest that it represents process B from the impedance measurements. This is another indicator that process A might be a grain boundary instead of a bulk process, otherwise we would expect to see two processes in the NMR results. In addition, a single ion transport process in the bulk is another reason to classify process C as an artefact. Regarding the activation energies, Lunghammer has deduced a value of 0.26 eV from the high-temperature flank of the $T_{1\rho}$ measurements. As it is less influenced by non-diffusive effects, the high-temperature flank provides the most reliable estimate for the activation energy. It deviates from the activation energy determined for the bulk process in the impedance measurement (0.43 and 0.49 eV). A reason for this could be that NMR relaxation measurements, even in this temperature range, probe local jumps while impedance measurements are sensitive to long-range transport. Once more, there is neither an activation energy derived from the NMR measurements comparable to the one assigned to process A (0.67 and 0.72 eV) nor one similar to the activation energy of a potential process C (0.03 eV), indicating that there is only one bulk process.

4.4 Comparison with previous studies

After determining the diffusion processes in our sample and their respective activation energies, we are interested in possible connections to the lithium diffusion models for $Li_2Ti_3O_7$ discussed in literature (section 2.2). In 2016, Islam *et al.*[11] published a study in which they calculated DFT (Density Functional Theory) models of ramsdellite $Li_2Ti_3O_7$. Focusing on the most energetically favourable ones, they compared the energy difference ΔE between neighbouring sites and calculated the theoretical activation energy E_a necessary for jump processes between them. Islam *et al.* found significant differences in the energy landscape in the ac-plane compared to the b-axis, the direction of the tunnels. Energy levels of crystal sites along migration paths in the plane vary more strongly, as schematically depicted in Figure 27. Consequently, the energetically favourable sites, once occupied, do impede further jumps of an atom and hereby hamper its migration. Islam *et al.* concluded that a diffusion along the plane is kinetically unfavourable, indicating that $Li_2Ti_3O_7$ is in fact a quasi-1D ion conductor.[11] This assumption is supported by experiments conducted by Wiedemann *et al.*[19], who used neutron diffraction to determine the position of lithium atoms in the $Li_2Ti_3O_7$ framework and found that they predominantly occupy sites inside the channels.

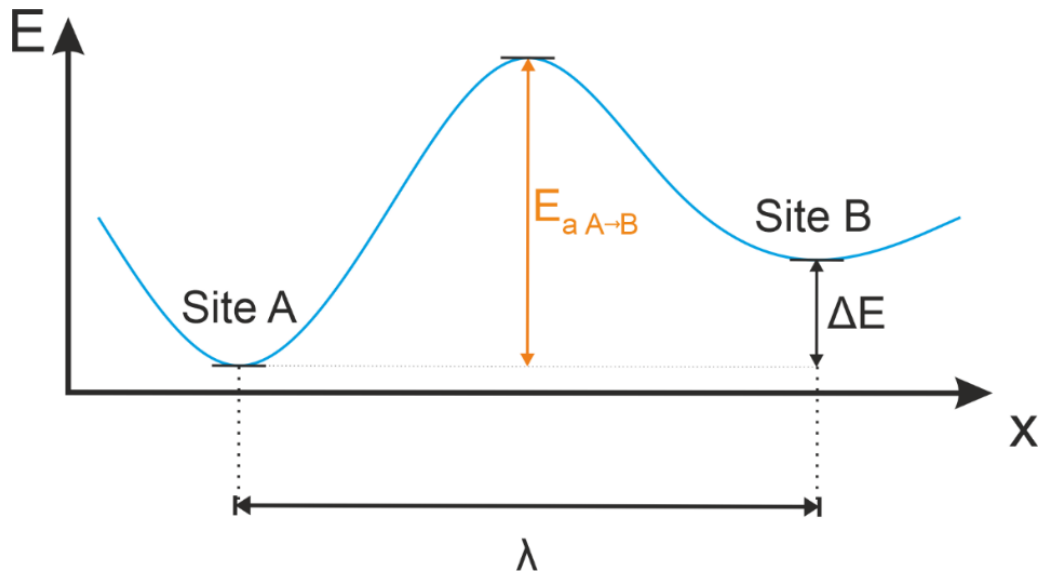

Figure 27: Energy landscape between two distinct crystal sites A and B. The probability of an atom transfer from one to the other is defined by the needed activation energy E_a as well as the energy difference ΔE between the sites. The transition from site A to site B is energetically less favorable than the reverse one. Figure inspired by reference 21.

When we compare our experimental results to the theoretical ones of Islam *et al*., in terms of activation energy the bulk process of our sample (0.43 and 0.49 eV, consistent with experimental literature values of 0.47 eV for bulk diffusion along the b-axis[41]) would fit the calculated activation energies of the lithium migration via unoccupied sites of the channels (0.20 − 0.92 eV). The low energy differences between the sites (0.10 – 0.35 eV) do imply that this is the preferred migration pathway. Migration along the ac-plane, according to their models, would require a similar activation energy (0.58 – 0.85 eV). Though this might be close to the E_a of the bulk and even includes the range of our assumed grain boundary process around 0.7 eV, ΔE is larger (0.56 – 0.73 eV), hereby decreasing the probability of consecutive jumps in the plane. The presence of Li defects in the material reduces Δ*E,* down to a range where the bulk process could be a result of migrations along the ac-plane via defects. However, the quantity of these defects inside the material is expected to be low, especially because of the annealing step after milling of the sample in our synthesis. The unidentified process C has no counterpart in the proposed pathways. It´s comparably small activation energy of 0.03 eV and the high frequency range on which it occurs might point to attempted jump processes or some localized jumps, for example an exchange between the 4c and 8d positions in the channels. More likely, they could represent lattice vibrations or artefacts of the high frequency measurement.

5 Conclusions

In this thesis, the analysis of EIS measurements points to two distinct Li^+ diffusion processes in ramsdellite $Li_2Ti_3O_7$, observed at temperatures ranging from −100 °C to 200 °C. On the one hand, we have a process in the mHz to kHz range that we characterise as a grain boundary process, although some investigated properties are close to those of a bulk process. Therefore, a definite classification would require additional analyses. On the other hand, we observed a bulk process in a frequency range from 10 Hz to 10 MHz. As lithium-ion diffusion through the bulk is of special importance for understanding the transport mechanism within the channel structure of ramsdellite $Li_2Ti_3O_7$, we put our emphasis on this type of process. ^{7}Li NMR relaxation measurements point to a single transport process in the bulk of the sample. While the activation energies derived from these measurements deviate from our findings (presumably based on the different methods used), a comparison with other literature references shows that multiple studies have found similar activation energies for a bulk process. In order to characterise the dimensionality of the bulk process, we used the universal power law proposed by A. Jonscher. However, the power law exponents *n* derived from our fits do not fulfil the criteria of a 1D (below 0.4) or 2D (below 0.6) ion conductor. We attribute this deviation to the fact that the power law is based on empirical observation and might therefore not apply to our material, therefore not giving more insights into the dimensionality.

At high frequencies, around 0.4 GHz, we detect a potential third process (C). We derive a small activation energy (0.03 eV) from the DC conductivities, but none from the modulus spectra as we do not observe a frequency-dependence. The low activation energy combined with the high frequency at which process C occurs suggests a fast, local jump process, maybe between energetically similar lithium positions within the channels. It could also originate from lattice vibrations or unsuccessful jumps. In addition, we must also consider the possibility of an artefact from the high-frequency impedance measurement.

6 List of figures

7 References

(1) *World Energy Outlook 2024*; Cozzi, L., Gould, T., Series Eds.; International Energy Agency: Paris, **2024**. https://www.iea.org/reports/world-energy-outlook-2024.

(2) Guan, Y.; Yan, J.; Shan, Y.; Zhou, Y.; Hang, Y.; Li, R.; Liu, Y.; Liu, B.; Nie, Q.; Bruckner, B.; Feng, K.; Hubacek, K. Burden of the Global Energy Price Crisis on Households. *Nat. Energy* **2023**, *8* (3), 304–316. https://doi.org/10.1038/s41560-023-01209-8.

(3) *Global Energy Crisis*; International Energy Agency, **2022**. https://www.iea.org/topics/global-energy-crisis.

(4) Nassar, Y.; Khaleel, M. Sustainable Development and the Surge in Electricity Demand Across Emerging Economies. *Int. J. Electr. Eng. Sustain.* **2024**, *2* (1), 51–60.

(5) Khan, T.; Garg, A. K.; Gupta, A.; Madan, A. K.; Jain, P. K. Comprehensive Review on Latest Advances on Rechargeable Batteries. *J. Energy Storage* **2023**, *57*, 106204. https://doi.org/10.1016/j.est.2022.106204.

(6) Zhao, L.; Ding, B.; Qin, X.; Wang, Z.; Lv, W.; He, Y.; Yang, Q.; Kang, F. Revisiting the Roles of Natural Graphite in Ongoing Lithium-Ion Batteries. *Adv. Mater.* **2022**, *34* (18), 2106704. https://doi.org/10.1002/adma.202106704.

(7) Persson, K.; Sethuraman, V. A.; Hardwick, L. J.; Hinuma, Y.; Meng, Y. S.; Van Der Ven, A.; Srinivasan, V.; Kostecki, R.; Ceder, G. Lithium Diffusion in Graphitic Carbon. *J. Phys. Chem. Lett.* **2010**, *1* (8), 1176–1180. https://doi.org/10.1021/jz100188d.

(8) Yi, T.-F.; Wei, T.-T.; Li, Y.; He, Y.-B.; Wang, Z.-B. Efforts on Enhancing the Li-Ion Diffusion Coefficient and Electronic Conductivity of Titanate-Based Anode Materials for Advanced Li-Ion Batteries. *Energy Storage Mater.* **2020**, *26*, 165–197. https://doi.org/10.1016/j.ensm.2019.12.042.

(9) Zhu, G.-N.; Wang, Y.-G.; Xia, Y.-Y. Ti-Based Compounds as Anode Materials for Li-Ion Batteries. *Energy Environ. Sci.* **2012**, *5* (5), 6652. https://doi.org/10.1039/c2ee03410g.

(10) Díaz-Carrasco, P.; Miscow Ferreira, P. C.; Dolotko, O.; Pérez-Flores, J. C.; Amador, U.; Kuhn, A.; García-Alvarado, F. The Effect of Ceramic Synthesis Conditions on the Electrochemical Properties of Li2Ti3O7. *J. Mater. Sci.* **2016**, *51* (9), 4520–4529. https://doi.org/10.1007/s10853-016-9764-3.

(11) Islam, M. M.; Heitjans, P.; Bredow, T. Structural Analysis and Li Migration Pathways in Ramsdellite $Li_2 Ti_3 O_7$: A Theoretical Study. *J. Phys. Chem. C* **2016**, *120* (1), 5–10. https://doi.org/10.1021/acs.jpcc.5b07942.

(12) Abrahams, I.; Bruce, P. G.; David, W. I. F.; West, A. R. Refinement of the Lithium Distribution in Li2Ti3O7 Using High-Resolution Powder Neutron Diffraction. *J. Solid State Chem.* **1989**, *78* (1), 170–177. https://doi.org/10.1016/0022-4596(89)90141-2.

(13) Morosin, B.; Mikkelsen Jnr, J. C. Crystal Structure of the Li+ Ion Conductor Dilithium Trititanate, Li2Ti3O7. *Acta Crystallogr. B* **1979**, *35* (4), 798–800. https://doi.org/10.1107/S0567740879004921.

(14) Dompablo, M.; García, J.; Várez, A.; García-Alvarado, F. Electrode Characteristics of Li2Ti3O7-Ramsdellite Processed by Mechanical Grinding. *J. Mater. Sci.* **2002**, *37* (18), 3981–3986. https://doi.org/10.1023/A:1019688413180.

(15) De Dompablo, M.; Morán, E.; A. Várez; García-Alvarado, F. Electrochemical Lithium Intercalation in Li2Ti3O7-Ramsdellite Structure. *Mater. Res. Bull.* **1997**, *32* (8), 993–1001. https://doi.org/10.1016/S0025-5408(97)00080-9.

(16) Van Der Ven, A. Lithium Diffusion in Layered Li[Sub x]CoO[Sub 2]. *Electrochem. Solid-State Lett.* **1999**, *3* (7), 301. https://doi.org/10.1149/1.1391130.

(17) Kuhn, A.; Sreeraj, P.; Pöttgen, R.; Wiemhöfer, H.-D.; Wilkening, M.; Heitjans, P. Li Ion Diffusion in the Anode Material $Li_{12} Si_7$: Ultrafast Quasi-1D Diffusion and Two Distinct Fast 3D Jump Processes Separately Revealed by ^{7}Li NMR Relaxometry. *J. Am. Chem. Soc.* **2011**, *133* (29), 11018–11021. https://doi.org/10.1021/ja2020108.

(18) Orera, A.; Azcondo, M. T.; García-Alvarado, F.; Sanz, J.; Sobrados, I.; Rodríguez-Carvajal, J.; Amador, U. Insight into Ramsdellite Li_2 Ti_3 O_7 and Its Proton-Exchange Derivative. *Inorg. Chem.* **2009**, *48* (16), 7659–7666. https://doi.org/10.1021/ic900398j.
(19) Wiedemann, D.; Nakhal, S.; Franz, A.; Lerch, M. Lithium Diffusion Pathways in Metastable Ramsdellite-like Li2Ti3O7 from High-Temperature Neutron Diffraction. *Solid State Ion.* **2016**, *293*, 37–43. https://doi.org/10.1016/j.ssi.2016.06.002.
(20) Lunghammer, S. Hochauflösende NMR-Messungen an Kanalstrukturiertem Li2Ti3O7 Und Dem Orthosilikat Li4SiO4. Master thesis, Graz University of Technical, Graz, **2016**.
(21) Mehrer, H. *Diffusion in Solids: Fundamentals, Methods, Materials, Diffusion-Controlled Processes*; Springer series in solid state science; Springer: Berlin New York, **2007**.
(22) Fick, A. Ueber Diffusion. *Ann. Phys.* **1855**, *170* (1), 59–86. https://doi.org/10.1002/andp.18551700105.
(23) Garnier, S. Electrochemical Intercalation of Lithium into the Ramsdellite-Type Structure of Li2Ti3O7. *Solid State Ion.* **1996**, *83* (3–4), 323–332. https://doi.org/10.1016/0167-2738(96)00002-1.
(24) Morosin, B.; Mikkelsen Jnr, J. C. Crystal Structure of the Li+ Ion Conductor Dilithium Trititanate, Li2Ti3O7. *Acta Crystallogr. Sect. B Struct. Sci. Cryst. Eng. Mater.* **1979**, *B35*, 798–800. https://doi.org/10.1107/S0567740879004921.
(25) Aldon, L.; Vanthournout, M.; Strobel, P.; Isnard, O.; Olivierfourcade, J.; Jumas, J. Neutron Diffraction and Mössbauer Studies of Iron Substituted Li2Ti3O7 of Ramsdellite-Type as Negative Electrode for Li-Ion Accumulator. *Solid State Ion.* **2006**, *177* (13–14), 1185–1191. https://doi.org/10.1016/j.ssi.2006.03.029.
(26) Woolfson, M. M. *An Introduction to X-Ray Crystallography*, Second edition.; Cambridge University Press: Cambridge, **1997**. https://doi.org/10.1017/CBO9780511622557.
(27) Lazanas, A. Ch.; Prodromidis, M. I. Electrochemical Impedance Spectroscopy–A Tutorial. *ACS Meas. Sci. Au* **2023**, *3* (3), 162–193. https://doi.org/10.1021/acsmeasuresciau.2c00070.
(28) Lvovich, V. F. *Impedance Spectroscopy: Applications to Electrochemical and Dielectric Phenomena*, 1st ed.; Wiley, **2012**. https://doi.org/10.1002/9781118164075.
(29) Jonscher, A. K. The 'Universal' Dielectric Response. *Nature* **1977**, *267* (5613), 673–679. https://doi.org/10.1038/267673a0.
(30) Sidebottom, D. L. Dimensionality Dependence of the Conductivity Dispersion in Ionic Materials. *Phys. Rev. Lett.* **1999**, *83* (5), 983–986. https://doi.org/10.1103/PhysRevLett.83.983.
(31) Jodlbauer, A.; Spychala, J.; Hogrefe, K.; Gadermaier, B.; Wilkening, H. M. R. Fast Li Ion Dynamics in Defect-Rich Nanocrystalline Li_4 PS_4 I–The Effect of Disorder on Activation Energies and Attempt Frequencies. *Chem. Mater.* **2024**, *36* (3), 1648–1664. https://doi.org/10.1021/acs.chemmater.3c02988.
(32) Irvine, J. T. S.; Sinclair, D. C.; West, A. R. Electroceramics: Characterization by Impedance Spectroscopy. *Adv. Mater.* **1990**, *2* (3), 132–138. https://doi.org/10.1002/adma.19900020304.
(33) Barsoukov, E. *Impedance Spectroscopy: Theory, Experiment, and Applications*, 2nd ed.; John Wiley & Sons, Incorporated: Hoboken, **2005**.
(34) Stainer, F.; Gadermaier, B.; Kügerl, A.; Ladenstein, L.; Hogrefe, K.; Wilkening, H. M. R. Fast Na+ Ion Dynamics in the Nb5+ Bearing NaSICON Na3+−Nb Zr2−Si2+P1−O12 as Probed by 23Na NMR and Conductivity Spectroscopy. *Solid State Ion.* **2023**, *395*, 116209. https://doi.org/10.1016/j.ssi.2023.116209.
(35) Xiang, Y.-X.; Zheng, G.; Zhong, G.; Wang, D.; Fu, R.; Yang, Y. Toward Understanding of Ion Dynamics in Highly Conductive Lithium Ion Conductors: Some Perspectives by Solid State NMR Techniques. *Solid State Ion.* **2018**, *318*, 19–26. https://doi.org/10.1016/j.ssi.2017.11.025.
(36) Wilkening, M.; Heitjans, P. From Micro to Macro: Access to Long-Range Li^+ Diffusion Parameters in Solids via Microscopic^{6,7} Li Spin-Alignment Echo NMR Spectroscopy. *ChemPhysChem* **2012**, *13* (1), 53–65. https://doi.org/10.1002/cphc.201100580.

(37) Ogihara, T.; Kodera, T. Synthesis of Li2Ti3O7 Anode Materials by Ultrasonic Spray Pyrolysis and Their Electrochemical Properties. *Materials* **2013**, *6* (6), 2285–2294. https://doi.org/10.3390/ma6062285.
(38) Heine, J. NMR- und impedanzspektroskopische Untersuchungen an Lithium-Ionenleitern mit eingeschränkter Dimensionalität der Diffusion. Doctoral dissertation, Gottfried-Wilhelm-Leibniz Universität, Hannover, **2020**.
(39) Gadermaier, B.; Stanje, B.; Wilkening, A.; Hanzu, I.; Heitjans, P.; Wilkening, H. M. R. Glass in Two Forms: Heterogeneous Electrical Relaxation in Nanoglassy Petalite. *J. Phys. Chem. C* **2019**, *123* (15), 10153–10162. https://doi.org/10.1021/acs.jpcc.9b01423.
(40) Zhang, L.; Dai, Y.; Li, C.; Dang, Y.; Zheng, R.; Wang, Z.; Wang, Y.; Cui, Y.; Arandiyan, H.; Shao, Z.; Sun, H.; Zhuang, Q.; Liu, Y. Recent Advances in Electrochemical Impedance Spectroscopy for Solid-State Batteries. *Energy Storage Mater.* **2024**, *69*, 103378. https://doi.org/10.1016/j.ensm.2024.103378.
(41) Boyce, J. B.; Mikkelsen, J. C. Anisotropic Conductivity in a Channel-Structured Superionic Conductor: Li2Ti3O7. *Solid State Commun.* **1979**, *31* (10), 741–745. https://doi.org/10.1016/0038-1098(79)90780-4.

8 Appendix

8.1 Jonscher fit correction

By extending the semi-circle of process A with a linear fit, as depicted in Figure 28 A, the resistive contribution of process B can be estimated, as the point of intersection of the fit with the x-axis yields its maximum resistance *R*. The frequency at which it occurs is identical to that of the DC plateau but may differ from the frequency at which the maximum of tan*(δ)* is located (Δ*v*; Figure 28 B). As the conductivity at this frequency could differ from the σ_{DC} value derived from $\tan(\delta)_{max}$ and can be used as an alternative starting point for σ_{DC} in a Jonscher fit (Jonscher fit_{corr}).

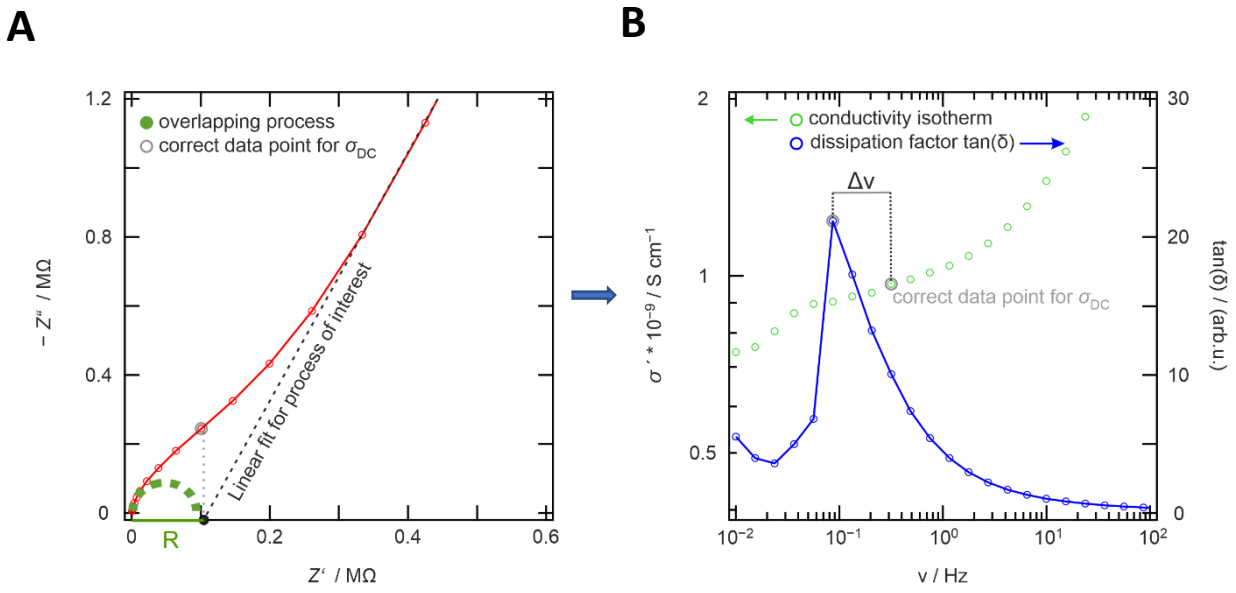

Figure 28: A linear fit of the investigated process in the Nyquist plot is used to distinguish it from an overlapping additional process (green) and identify the data point at which the process of interest would start without the overlap (A). This data point is then used to find σ_{DC} of the process in the corresponding conductivity isotherm (B). As the conductivity σ_{DC} for the original Jonscher fits is taken at the frequency where the tan(δ) has its maxima, the correction can lead to different values for σ_{DC}, depending on the plateau.

Acknowledgement

I would like to thank professor Wilkening for allowing me to conduct my master thesis under his supervision, providing the organisational and financial framework for my thesis as well as the opportunity to develop a deeper understanding of the subject matter. Many thanks also to my colleagues at the ICTM institute for their support and encouragement throughout the process. Special mention must be given to Dipl.-Ing. Annika Marko, who patiently took the time to guide me through the challenges of a scientific thesis and kept me from indiscriminately pursuing every idea I had regarding my data set.

I am tremendously grateful to my family for their love and support over the years, prior to and during my time at university. To my parents Hartwig and Margit, my sister Larissa and my aunt and uncle, Klaudia and Franz, I could not have chosen and followed this path without you.

Last, but certainly not least, I want to thank the amazing group of friends that I am lucky enough to be surrounded by throughout the highs and lows of everyday existence, on and off campus. They know who they are and that I love them. Thank you for accompanying, helping and criticising me along my journey so far and for letting me take part in yours.

Für meine Oma, Ernestine Kreiseder.

Danke!

Danke für Deine Zeit, Deine Aufmerksamkeit, Deine Sorge um mich (wenn auch hin und wieder etwas übertrieben) und Deine Fürsorge. Für Dein offenes Ohr bezüglich meiner Pläne und Ängste. Danke für die Ratschläge und Lebensweisheiten, die Du mir vermittelt hast. Für Dein Vertrauen in mich. Für Dein Mitfiebern bei jeder neuen Herausforderung, sowie Deine Freude über jeden meiner Erfolg, die mir manchmal so viel größer erschien als meine Eigene. Auch daraus kann ich etwas lernen. Danke für Deine Stärke und Willenskraft. Und ich könnte noch so viel mehr schreiben.

Ich weiß, wie sehr Du Dich schon auf meinen Masterabschluss gefreut hast. Wie sehr du mit mir und für mich gefreut hast. Über meine Leistungen, die eigentlich unsere Leistungen sind, weil ich ohne Deine Unterstützung und auch Deine unermüdliche Ermutigung, etwas zu tun und zu schaffen, diese Zeilen heute nicht schreiben könnte. Also auch Gratulation an Dich! Wir haben es geschafft. Du hast mir diesbezüglich oft gesagt: „Den Letzten beißen die Hunde." Ich denke, das kann stimmen, aber genauso, dass man trotz aller Bemühungen von Zeit zu Zeit gebissen werden wird. Sogar, wenn man die/der Allerschnellste ist. Unabhängig davon gibt es auf dem Weg so viel zu bewundern. Auch das habe ich von Dir gelernt.

Ich hab Dich lieb.